

VALIDATION OF BIO-OPTICAL ALGORITHMS USING SATELLITE AND IN SITU RADIOMETRIC MEASUREMENTS FOR DERIVING COLOURED DISSOLVED ORGANIC MATTER (CDOM) IN THE KATTEGAT

Frida Björkroth



Figure 1: The in-water instrument, part of the in situ Open-source SpectroRadiometer (Open-SpecRad) system.

Degree project for Master of Science (120 hp) with a major in Marine Sciences
MAR703, Exam course for Master's degree in Marine Science - Chemistry, 60 hp
Second Cycle

Semester/year: Spring 2020

Supervisor: Martin Hassellöv, Department of Marine Sciences

Examiner: Katarina Abrahamsson, Department of Marine Sciences

Validering av bio-optiska algoritmer för beräkning av humusämnen i Kattegatt

Satellitbaserad fjärranalys av havsfärg innebär att mäta solljuset som spridits tillbaka upp från havsvattnet efter att ha interagerat med vattnet och dess innehåll. De huvudsakliga optiskt aktiva beståndsdelarna, klorofyll-a, humusämnen och lösta partiklar, har olika egenskaper som påverkar vilka färger (våglängder) av ljuset som absorberas eller sprids. Därför innehåller ljuset information om mängd och om vilka av beståndsdelarna som finns där. Intresset för humusämnen har nyligen ökat, eftersom man vill uppskatta det globalt lösta kolet i havet för bättre förståelse av kolcykeln. Mätning av löst kol är tidskrävande och kostsamt, så därför kan humusämnen användas för att uppskatta kolmängden. Humusämnen absorberar blått ljus och ser därför gula ut i vatten. Genom bio-optiska algoritmer, som kopplar ihop biologiska och optiska egenskaper, kan mängden av beståndsdelarna beräknas från satellitmätningar av ljuset. De globala algoritmerna som används idag fungerar bra i optiskt enkla vatten, där klorofyll-a dominerar, men misslyckas i optiskt komplicerade vatten, där humusämnen och lösta partiklar dominerar. Därför har enkla regionala algoritmer som baseras på förhållandet mellan två olika våglängdsband utvecklats.

En av de senaste sensorerna för fjärranalys av havsfärg är Ocean and Land Color Instrument (OLCI) ombord på satelliterna Sentinel-3A och 3B. Dess våglängdsband är speciellt utvalda för övervakning av optiskt komplicerade kustvatten. Validering och uppskattning av osäkerheter från olika vattenmiljöer är avgörande för tillförlitlig data från OLCI. Detta görs genom jämförelse mellan sammanfallande satellitmätningar och mätningar på plats i eller precis ovanför vattnet. Dock har aldrig ljusmätningarna från OLCI med fokus på humusämnen validerats omfattande i Kattegatt. Därför jämfördes mätningar av humusämnen på plats i Kattegatt med lokalt anpassade algoritmer applicerade på mätningar från ett egenbyggt optiskt instrument (Open-source SpectroRadiometer system, OpenSpecRad) och OLCI satellitmätningar. Resultaten visar att mängden humusämnen förutspått av algoritmerna inte hade något förhållande till den verkliga mängden humusämnen, på grund av stor tidsskillnad mellan satellitmätning och mätning på plats i lokala anpassningen av algoritmerna, orsakat av molntäcke. För första gången visas det att OLCI-dataprodukten för färgat detritus och löst material, ADG443, inte hade något förhållande till mätningar av humusämnen på plats.

Molntäcken är den största svagheten med satellitbaserad fjärranalys i Kattegatt, liksom i resten av norra Europa. ADG443 rekommenderas inte att användas för att uppskatta mängden humusämnen i Kattegatt. I framtiden skulle satellitbaserad fjärranalys av havsfärg kunna öka tillgängligheten av mätningar av humusämnen och användas i övervakning av vattenkvalitet. OpenSpecRad är billig och fritt tillgänglig för vem som helst att bygga, vilket utmanar gränserna för vem som kan bidra till vetenskapen.

Abstract

Satellite remote sensing of ocean color involves deriving the water-leaving radiance (L_w), which is the spectrum of sunlight backscattered out of the ocean after interaction with the water and its constituents. The L_w holds quantitative and qualitative information about the main optically active components of seawater, i.e. chlorophyll-a (Chl-a), coloured dissolved organic matter (CDOM), and total suspended matter (TSM). The interest in CDOM has recently increased due to the estimation of the global dissolved organic carbon (DOC) pool for the understanding of the changing carbon cycle. The global bio-optical algorithms and processors deriving water quality components from L_w perform well in optically simple Case-1 waters, dominated by Chl-a, but they fail in Case-2 waters, dominated by CDOM and TSM. Therefore, regional empirical algorithms, which depend on the ratio of two water-leaving reflectances (ρ_w) (derived from L_w) at different wavelengths, have been developed for determination of the absorbance coefficient for CDOM at wavelength 443 nm, $a_{CDOM}(443)$. However, there has been no considerable validation of the data from the new Ocean and Land Colour Instrument (OLCI) onboard the Sentinel-3 satellites nor regional empirical algorithms in the Kattegat. This study shows that $a_{CDOM}(443)$ predicted by the local algorithms has no correlation with in situ data, due to the large time difference between satellite overpass and in situ measurements in the local fitting of algorithms caused by cloud coverage. For the first time, it is also shown that the OLCI product for coloured detritus and dissolved matter, ADG443, has no correlation with $a_{CDOM}(443)$ in the Kattegat. Here, a self-built in situ Open-Source SpectroRadiometer (OpenSpecRad) system is also developed. The cloud coverage is the main weakness of satellite remote sensing in the Kattegat, as well as in northern Europe. Further, the ADG443 product is not recommended for using as a proxy for $a_{CDOM}(443)$ in the Kattegat. In the future, satellite remote sensing in the Kattegat could immensely increase the data availability for CDOM estimation and be used in water quality monitoring. The OpenSpecRad system is low-cost and free for anyone to build, hence pushing the limits for who can contribute to science.

Contents

1	Introduction	1
1.1	Inherent and Apparent Optical Properties	3
1.2	Satellite Remote Sensing of Ocean Colour	6
1.2.1	Sentinel-3 Ocean and Land Colour Instrument (OLCI)	9
1.2.2	Processing Levels and Data Products	9
1.3	In Situ Radiometric Measurements	12
1.3.1	In-Water Spectral Corrections	14
1.4	Requirements for the OpenSpecRad	15
1.5	Bio-optical Algorithms	16
1.6	Validation Statistics	17
2	Materials and Method	18
2.1	Bio-optical Algorithms	18
2.1.1	Fitting	18
2.1.2	Validation	18
2.2	OpenSpecRad Development	20
2.2.1	Performance Testing	20
2.2.2	Spectroradiometer Calibrations	20
2.3	OpenSpecRad Measurement and CDOM Analysis	21
2.3.1	Spectral Processing and Bio-optical Algorithm Validation	22
3	Result and Discussion	23
3.1	Sentinel-3 OLCI: Bio-optical Algorithm Validation	23
3.2	Usage and Performance of the OpenSpecRad	24
3.3	OpenSpecRad: Bio-optical Algorithm Validation	27
4	Conclusion	30
	Acknowledgements	31
	References	31
	Appendix A Building the OpenSpecRad	38

A.1	Hardware Assembly	38
A.2	Software Configurations	40
A.3	Housing and Frame Construction	41

Symbols and Abbreviations

Symbol	Unit	Description
0^-	m	Just under the sea surface
0^+	m	Just above the sea surface
A	m^2	Spherical surface area
a	m^{-1}	Absorption coefficient
B	unit-less	Function used in self-shading correction, depends on wavelength and sun zenith angle
b	m^{-1}	Total scattering coefficient
b_b	m^{-1}	Backscattering coefficient
$\beta(\theta)$	$\text{m}^{-1}\text{sr}^{-1}$	Volume scattering function
C_s		Coefficient describing variation in Sun-Earth distance
E	W m^{-3}	Irradiance
E_d	W m^{-3}	Downwelling irradiance
E_u	W m^{-3}	Upwelling irradiance
ϵ		Error
F_0	W m^{-3}	Mean solar spectral irradiance at the top of the atmosphere
F_i	unit-less	Immersion correction factor
f	unit-less	Self-shading correction factor
K_d	m^{-1}	Diffuse attenuation coefficient of downwelling irradiance
K_l	m^{-1}	Diffuse attenuation coefficient of upwelling radiance
$K_{\mathfrak{P}}$	m^{-1}	Diffuse attenuation coefficient, i.e $K_l(\lambda)$, $K_d(\lambda)$ and $K_u(\lambda)$ calculated from $L_u(z, \lambda)$, $E_d(z, \lambda)$ and $E_u(z, \lambda)$, respectively
K_u	m^{-1}	Diffuse attenuation coefficient of upwelling irradiance
L	$\text{W sr}^{-1} \text{m}^{-3}$	Radiance
L_i	$\text{W sr}^{-1} \text{m}^{-3}$	Sky radiance
L_T	$\text{W sr}^{-1} \text{m}^{-3}$	Total radiance emerging from sea surface
L_u	$\text{W sr}^{-1} \text{m}^{-3}$	Upwelling radiance
L_w	$\text{W sr}^{-1} \text{m}^{-3}$	Water-leaving radiance
L_{wn}	$\text{W sr}^{-1} \text{m}^{-3}$	Normalized water-leaving radiance
λ	nm	Wavelength
μ_s	$^\circ$	Cosine of the solar zenith angle
n_g, n_w	unit-less	Refractive indices of glass window and seawater, respectively
Ω	sr	Solid angle
$\Delta\Phi$	$^\circ$	Difference between sun and sensor azimuth angle
\mathfrak{P}		Radiometric parameters (L_u , E_d or E_u)
Q, Q_n		Q-factors describing anisotropy (dependency of direction)

$\mathfrak{R}, \mathfrak{R}_0$		Describing sea surface reflectance and refraction
R_{rs}	sr^{-1}	Remote sensing reflectance
r	m	Radius
ρ_w	unit-less	Water-leaving reflectance
t, t_0		Time and start time, respectively
t_{down}	unit-less	Downward transmittance of the atmosphere
τ_a	unit-less	Aerosol optical thickness
θ'	$^\circ$	Angle from zenith
θ_0	$^\circ$	Sun zenith angle
θ	$^\circ$	Angle from nadir
W	ms^{-1}	Windspeed
z	m	Depth

Abbreviation	Description
ADG443	OLCI satellite-derived absorption of coloured detritus and dissolved matter at 443 nm
AC	Atmospheric correction
AAC	Alternative atmospheric correction
ABS	Acrylonitrile butadiene styrene
AOP	Apparent optical property
APD	Average percentage difference
API	Application programming interface
BAC	Baseline atmospheric correction
C2RCC	Case-2 Regional CoastColour algorithm
CAD	Computer-aided design
CCD	Charge-coupled device
CDOM	Coloured dissolved organic matter
Chl-a	Chlorophyll-a
CZCS	Coastal Zone Color Sensor
DC	Digital counts
ESA	European Space Agency
EUMETSAT	European Organisation for the Exploitation of Meteorological Satellites
FAFOV	Full-angle field-of-view
I ² C	Inter-integrated circuit
IDE	Integrated development environment
IOP	Inherent optical property
IP	Internet protocol

L0, L1, L2	Level 0, Level 1, Level 2
MERIS	Medium Resolution Imaging Spectrometer
MNB	Mean normalized bias
MODIS	Moderate Resolution Imaging Spectrometer
NOOBS	New Out Of Box Software
NRT	Near real-time
NTC	Non-time critical
OC4ME	Ocean Colour for MERIS algorithm
OLCI	Ocean and Land Colour Instrument
OpenSpecRad	Open-source Spectroradiometer
PLA	Polylactic acid
RMSE	Root mean square error
RPi	Raspberry Pi
RTC	Real-time clock
s	Standard deviation
SD	Secure digital
SeaWiFS	Sea-viewing Wide Field-of-view Sensor
SSH	Secure shell
TOA	Top-of-atmosphere
TSM	Total suspended matter
UAVs	Unmanned aerial vehicles

1 Introduction

Satellite remote sensing of ocean colour involves deriving the water-leaving radiance (L_w), which is the spectrum of sunlight backscattered out of the ocean after interaction with the water and its constituents (Groom et al., 2019). In the coastal ocean, the main optically significant components determining the ocean colour are chlorophyll-a (Chl-a), coloured dissolved organic matter (CDOM), and total suspended matter (TSM) (Koponen et al., 2007; Kratzer et al., 2014). Each component, as well as the water itself, has different inherent optical properties (IOPs) and absorbs and scatters different parts of the spectrum (Kiryliuk, 2019). Therefore, the L_w contains quantitative and qualitative information about the in-water constituents (Loisel et al., 2013). Their concentrations are derived using so-called bio-optical algorithms which are based on their IOPs (Kratzer and Moore, 2018).

Today, the global bio-optical algorithms and standard processors deriving water quality products perform well in optically simple open ocean (Case-1) waters, where the IOPs are dominated by Chl-a, but they fail in optically complex coastal and partially enclosed marine (Case-2) waters, dominated by CDOM and TSM (Kowalczyk et al., 2005; Matsushita et al., 2012; Seelye, 2014). Therefore, regional empirical and semi-analytical algorithms have been developed and evaluated for the determination of water quality products, e.g. in the Baltic Sea (Kowalczyk et al., 2010; Ligi et al., 2017; Toming et al., 2017). The empirical algorithms, also called band-ratio algorithms, only depend on the ratio of two water-leaving reflectances ρ_w (derived from L_w) at different wavelengths and therefore they are computationally fast and widely used (Ligi et al., 2017; Seelye, 2014).

The interest in CDOM, also known as gelbstoff, humic substance, yellow substance, or chromophoric dissolved organic matter, has recently increased, due to the current estimation of the global dissolved organic carbon (DOC) pool for the understanding of the carbon cycle under change (Koponen et al., 2007; Kowalczyk et al., 2010; Tian et al., 2012). CDOM is the optically active fraction of DOC and since DOC measurements are costly and time-consuming CDOM is often used as a proxy (Harvey et al., 2015; Kowalczyk et al., 2010; Mishra et al., 2017). In addition, CDOM plays a key role for a better understanding of the air-sea exchange of inorganic carbon species (CO, CO₂ and COS), the formation of reactive oxygen species, its impact on satellite remote sensing of primary production, and attenuation of ultraviolet light

in surface waters (Kowalczyk et al., 2010).

CDOM is dominated by humic and fulvic acids which originates from the degradation of terrestrial and aquatic plant matter and is primarily transported into coastal waters through rivers and estuaries (Seelye, 2014; Stedmon et al., 2003, 2010). Hence, the CDOM concentration is inversely related to the salinity (Højerslev et al., 1996). CDOM is ubiquitous in natural waters and has aromatic, carboxylic acid, and phenolic groups, shaping its optical signature (Brezonik et al., 2005). CDOM is optically characterized by its absorption coefficient (a_{CDOM}) and is primarily absorbing light in the ultraviolet (UV) and the blue regions (450-490 nm) of the spectrum (Bricaud et al., 1981). Its absorption decreases with increasing wavelength according to the exponential equation (Bricaud et al., 1981)

$$a_{CDOM}(\lambda) = a_{CDOM}(\lambda_0)e^{-S(\lambda-\lambda_0)} \quad (1)$$

where a_{CDOM} is the absorption coefficient at wavelength λ , λ_0 is the reference wavelength, and S is the slope factor (Kowalczyk et al., 2010).

Ocean colour was monitored for the first time by satellite remote sensing when the Coastal Zone Color Sensor (CZCS) was launched in 1978, proving the concept of measuring ocean productivity from space (Groom et al., 2019; Kyryliuk and Kratzer, 2019). The following decades several one-off sensors were launched, e.g. the Sea-viewing Wide Field-of-view Sensor (SeaWiFS), the Moderate Resolution Imaging Spectrometer (MODIS), and the Medium Resolution Imaging Spectrometer (MERIS) (Berthon et al., 2008). One of the most recent sensors, the Ocean and Land Colour Instrument (OLCI) on the Sentinel-3A and Sentinel-3B satellites is part of the Sentinel-3 mission led by the European Space Agency (ESA) and the European Organisation for the Exploitation of Meteorological Satellites (EUMETSAT) (Groom et al., 2019). The OLCI spectral configuration is especially designed for monitoring of coastal Case-2 waters (Donlon et al., 2012; Toming et al., 2017). The Sentinel-3 mission marks the beginning of consistent ocean colour observations of coastal waters in the following decades. However, validation and determination of uncertainties from different aquatic environments are crucial for reliable OLCI ρ_w and water quality products (Toming et al., 2017; Zibordi et al., 2012). This is performed by comparison of satellite products with in situ reference measurements (Zibordi et al., 2012).

The Kattegat Sea is part of the transition zone between the Baltic Sea and the North Sea. Its water originates from three different water masses, (1) low-salinity (8 PSU) Baltic Sea water with high a_{CDOM} , (2) high-salinity (35 PSU) North Sea water with low a_{CDOM} and (3) high-salinity (31 PSU) German Bight water with high a_{CDOM} (Højerslev et al., 1996; Stedmon et al., 2010). The Kattegat Sea bottom water is a mix of North Sea water (90%) and German bight water (10%) while the surface water is dominated by the Baltic Sea water, which flows northward along the Swedish coast (Björk and Nordberg, 2003; Højerslev et al., 1996). Previous CDOM studies in the Kattegat have been focusing on water mass mixing (Stedmon et al., 2010) and characterization of components (Osburn and Stedmon, 2011; Persson and Wedborg, 2001; Stedmon et al., 2003). Sørensen et al. (2007) performed a validation of MERIS data in the Skagerrak, with some sampling stations in the Kattegat. Although, there has been no extensive validation of the OLCI data products including CDOM in the Kattegat. Therefore, the aim of this study is to investigate the potentials of radiometric measurements and published bio-optical algorithms for water quality monitoring in the Kattegat with the focus on CDOM, using data from the Sentinel-3 OLCI satellites and a self-built in situ Open-source SpectroRadiometer (OpenSpecRad) system. Hence, this study also aims to build a low-cost in situ spectroradiometer system and can thereby be used as a handbook.

1.1 Inherent and Apparent Optical Properties

The inherent optical properties (IOPs) of seawater, i.e. the absorption coefficient (a), the scattering coefficient (b), and the volume scattering function ($\beta(\theta)$), only depend on the nature of the medium and are independent of the ambient light field (Kratzer et al., 2017; Preisendorfer, 1961). The intensity of light underwater reduces with increasing depth due to the absorption and scattering of the in-water components (Kratzer et al., 2014).

CDOM absorbs light predominantly in the blue (450-490 nm) part of the spectrum, whereas Chl-a absorbs light both in the blue and red (635-700 nm) part (Kratzer et al., 2014). TSM mainly scatters light, which means a photon changes its direction after interaction with the matter (Kratzer et al., 2014, 2017). Backscattered photons are photons that are reflected at angles less than 90° or $\pi/2$ radians.

For a given water body the absorption coefficient (a) of light can be described as

$$a(\lambda) = a_w(\lambda) + a_{Chl-a}(\lambda) + a_{CDOM}(\lambda) + a_{TSM}(\lambda), \quad (2)$$

the total scattering coefficient (b) of light as

$$b(\lambda) = b_w(\lambda) + b_{TSM}(\lambda), \quad (3)$$

and the backscattering coefficient (b_b) of light as

$$b_b(\lambda) = b_{bw}(\lambda) + b_{bTSM}(\lambda) \quad (4)$$

where λ is the wavelength and the subscripts w refers to clear water, Chl-a to chlorophyll-a, CDOM to coloured dissolved organic matter, and TSM to total suspended matter ([Kratzer and Moore, 2018](#); [Seelye, 2014](#)).

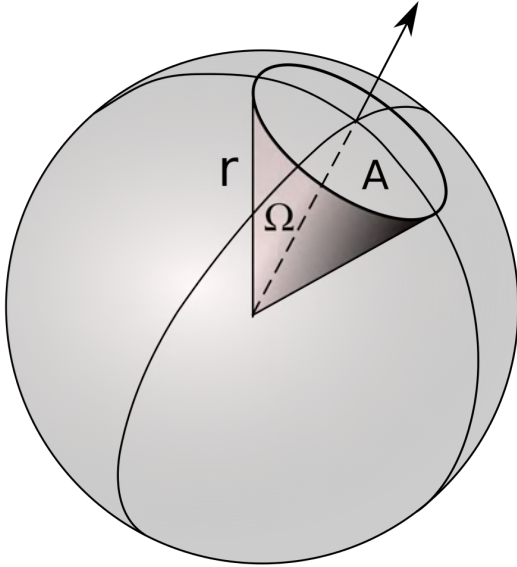


Figure 2: The solid angle (Ω) defined by the spherical surface area A and the radius of the sphere r, according to equation 5.

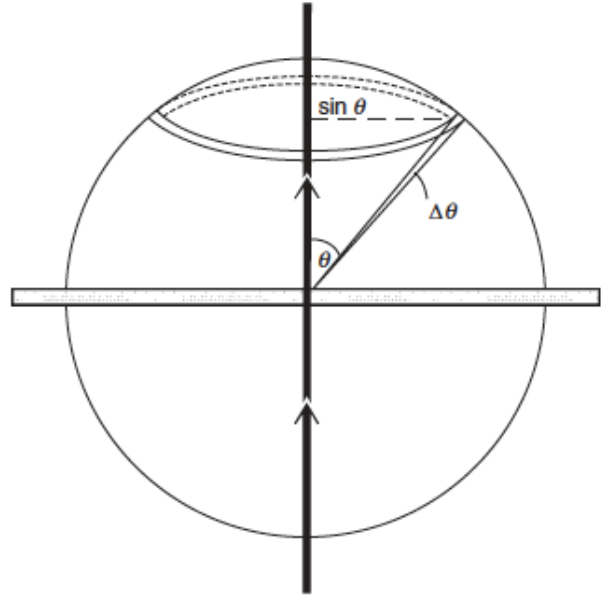


Figure 3: The differential solid angle ($d\Omega$) of a light beam, defined by the scattering angles θ to $\theta + \Delta\theta$ with radius $\sin(\theta)$, according to equation 6. Adopted from [Kirk \(2011\)](#).

Because particle scattering is directionally dependent, it is characterized by the volume scattering function ($\beta(\theta)$) ([Kratzer and Moore, 2018](#)). It describes how a given volume of water scatters incident light into different directions in a three-dimensional space. Firstly, the equivalent of the two-dimensional planar angle in a three-dimensional space is called the solid angle (Ω) (Fig. 2). It is the angular volume, often a cone, created by lines from a patch of

area on a sphere meeting at the centered apex and is defined as

$$\Omega = \frac{A}{r^2} \quad (5)$$

where A is the spherical surface area and r is the radius of the sphere (Seelye, 2014). The solid angle has unit steradian (sr), with 4π sr in a sphere, since the surface area of a sphere is $A = 4\pi r^2$ (Seelye, 2014). Secondly, the differential solid angle ($d\Omega$) can be explained as a light beam passing through a medium and is scattered between angle θ and $\theta + \Delta\theta$, enclosing an area with radius $\sin(\theta)$ according to

$$d\Omega = 2\pi \sin(\theta) d\theta \quad (6)$$

(Fig. 3) (Kirk, 2011).

Thereby, the $b(\lambda)$ is the integral of the $\beta(\theta, \lambda)$ over all Ω , according to

$$b(\lambda) = \int_{4\pi} \beta(\theta, \lambda) d\Omega \quad (7)$$

(Mobley, 1995). Combining equation 6 and 7 gives

$$b(\lambda) = 2\pi \int_0^\pi \beta(\theta, \lambda) \sin(\theta) d\theta \quad (8)$$

where $0 \leq \theta \leq \pi$ radians denote all directions. This means the $b_b(\lambda)$ is the integral over the backwards direction $\pi/2 \leq \theta \leq \pi$ radians as

$$b_b(\lambda) = 2\pi \int_{\pi/2}^\pi \beta(\theta, \lambda) \sin(\theta) d\theta \quad (9)$$

(Mobley, 1995). Backscattering is a crucial part of ocean optics since most of the light emerging upwards from the ocean is originally downward directed sunlight, which was redirected upwards (Kratzer et al., 2017). Together the absorption and backscattering form the colour of the oceans.

The CDOM absorption coefficient, $a_{CDOM}(\lambda)$, is derived using (Kirk, 2011; Kratzer and Moore, 2018):

$$a_{CDOM}(\lambda) = \ln(10)A(\lambda) / l \quad (10)$$

where A is the absorbance and l is the cuvette path length in cm. The a_{CDOM} is often calculated at wavelengths 412 or 420-443 nm (Brezonik et al., 2015).

In contrast to the IOPs, the apparent optical properties (AOPs) of seawater are both dependent on the medium and the ambient light field (Preisendorfer, 1961). The light field is quantified by the radiance (L) and the irradiance (E). Irradiance is how much light that hits a specified area and has unit watt per square meter per meter (W m^{-3}), more often as $\text{mW cm}^{-2} \text{ nm}^{-1}$ (Kirk, 2011; Zibordi et al., 2012). Radiance is how much light coming through a specified area and falling into a given solid angle in a defined direction and has unit watt per steradian per square meter per meter ($\text{W sr}^{-1} \text{ m}^{-3}$), often expressed as $\text{mW sr}^{-1} \text{ cm}^{-2} \text{ nm}^{-1}$ (Kratzer et al., 2017; Zibordi et al., 2012). One important AOP is the remote sensing reflectance $R_{rs}(\lambda)$. It is defined as the ratio of water-leaving radiance $L_w(\lambda)$ to downwelling irradiance $E_d(\lambda)$,

$$R_{rs}(\lambda) = \frac{L_w(\lambda)}{E_d(0^+, \lambda)} \quad (11)$$

where 0^+ is just above the sea surface (Kowalczyk et al., 2005; Zibordi et al., 2012). Both $L_w(\lambda)$ and $E_d(0^+, \lambda)$ are dependent on the illumination condition, e.g. sun elevation, clouds and atmospheric conditions, at the moment of measurement (Kratzer et al., 2017). Therefore, $R_{rs}(\lambda)$ is very useful since it is less sensitive to changes in sunlight. R_{rs} is also proportional to the absorption coefficient (a) and backscattering coefficient (b_b) according to

$$R_{rs} \propto \frac{b_b}{a + b_b} \quad (12)$$

(Kiryliuk, 2019).

Another common AOP is the diffuse attenuation coefficient of downwelling irradiance $K_d(z, \lambda)$, which is derived from the exponential decrease in $E_d(z, \lambda)$ with increasing depth (Eq. 13 and 14) (Kirk, 2011; Kratzer et al., 2017).

$$E_d(z, \lambda) = E_d(0^-, \lambda) \cdot e^{-K_d(\lambda) \cdot z} \quad (13)$$

$$K_d(z, \lambda) = \frac{-\left(\ln E_d(z, \lambda) - \ln E_d(0^-, \lambda)\right)}{z} \quad (14)$$

where z is the depth and 0^- is just below the sea surface (Kirk, 2011).

1.2 Satellite Remote Sensing of Ocean Colour

Satellite remote sensing of ocean colour includes detecting water-leaving radiance (L_w) as if it was measured in situ (Fig. 4) (Groom et al., 2019). However, satellite sensors in fact measure

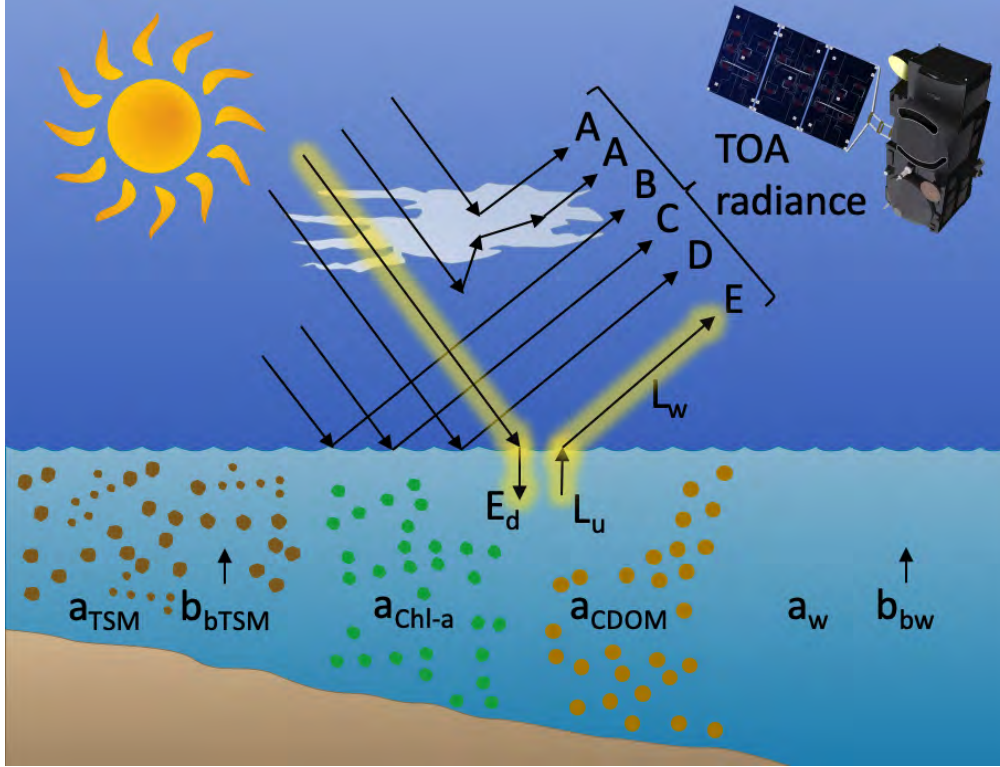


Figure 4: Components involved in remote sensing of ocean colour. The inherent optical properties (IOPs) absorption (a) and backscattering (b_b) with the subscript TSM referring to total suspended matter, Chl-a to chlorophyll-a, CDOM to coloured dissolved organic matter, and w to clear water. The top-of-atmosphere (TOA) stems from five key processes; A) Single and multiple atmospheric scattering by molecules and/or aerosols, B) atmospheric scattering reflected by the sea surface (sky glint), C) atmospheric scattering reflected by whitecaps at the sea surface D) specular (mirror-like) reflection of light by sea surface with direct transmission (sunglint) and E) transmission down through the atmosphere and air-sea interface (downwelling irradiance, E_d), interaction with water and its optical components and up through the sea-air interface (upwelling radiance, L_u refracted into L_w) and atmosphere. Adapted from [Kay et al. \(2009\)](#) and SkywalkerPL, [Creative Commons Attribution 4.0 International license](#)

the top-of-atmosphere (TOA) radiance ([Loisel et al., 2013](#)). The L_w is only about 10% of the measured TOA signal and even smaller in strongly absorbing waters ([Kratzer et al., 2017](#)). The remaining part of the signal (90%) is caused by light interacting with the atmosphere, with the largest contribution from atmospheric scattering. Thus, the TOA radiance must be measured with accuracy, since the residual errors will propagate to the L_w ([Groom et al., 2019](#)).

The TOA radiance stems from five key processes; A) Single and multiple atmospheric scattering by molecules and/or aerosols, B) atmospheric scattering reflected by the sea surface (sky glint), C) atmospheric scattering reflected by whitecaps at the sea surface D) specular (mirror-like)

Table 1: The Sentinel-3 Ocean and Land Colour Instrument (OLCI) wavelength band configuration, with band name, central wavelength, band width and main purpose in the data processing. All 21 bands are available through the level 1 (L1) data product, whereas only the bands marked with gray are included in the level 2 (L2) data product. From [EUMETSAT \(2018\)](#).

Band name	Central wavelength (nm)	Bandwidth (nm)	Main purpose
Oa1	400	15	AC
Oa2	412.5	10	CDOM
Oa3	442.5	10	Chl-a absorption maximum
Oa4	490	10	Chl-a
Oa5	510	10	Chl-a and TSM
Oa6	560	10	Chl-a minimum
Oa7	620	10	TSM
Oa8	665	10	Chl-a, TSM and CDOM
Oa9	673.75	7.5	Fluorescence
Oa10	681.25	7.5	Chl-a fluorescence
Oa11	708.75	10	Chl-a fluorescence
Oa12	753.75	7.5	Oxygen absorption and clouds
Oa13	761.25	2.5	Oxygen absorption and AC aerosol
Oa14	764.375	3.75	AC
Oa15	767.5	2.5	Oxygen absorption
Oa16	778.75	15	AC aerosol
Oa17	865	20	AC aerosol clouds
Oa18	885	10	Water vapour absorption
Oa19	900	10	Water vapour absorption
Oa20	940	20	Water vapour absorption and AC
Oa21	1020	40	AC aerosol

reflection of light by sea surface with direct transmission (sunglint) and E) transmission down through the atmosphere and air-sea interface (downwelling irradiance, E_d), interaction with water and its optical components and up through the sea-air interface (upwelling radiance, L_u refracted into L_w) and atmosphere (Fig. 4) ([Kay et al., 2009](#)).

In order to derive the L_w from TOA radiance, the atmospheric effects (paths A-D in Fig. 4) must first be modeled and then removed ([Kratzer and Moore, 2018](#)). This process is called atmospheric correction (AC) and is conducted in different ways depending on the sensor ([Kirk, 2011](#)). For the Ocean and Land Colour Instrument (OLCI) on the Sentinel-3A and Sentinel-3B satellites, the AC is performed on the last out of three processing levels.

1.2.1 Sentinel-3 Ocean and Land Colour Instrument (OLCI)

The Ocean and Land Colour Instrument (OLCI) on the Sentinel-3A and Sentinel-3B satellites is an optical instrument detecting the TOA radiance. The Sentinel-3 mission was planned to overlap with the MERIS mission (2002-2012), but due to several delays the Sentinel-3A was launched in 2016 and followed by the Sentinel-3B in 2018 (Groom et al., 2019; Kyryliuk, 2019). Two more Sentinel-3 satellites are planned to be launched until 2030 (Kyryliuk, 2019). The primary objective of the OLCI in the marine environment is to deliver high-quality ocean colour data products (EUMETSAT, 2018). This is of large interest in ocean colour studies since the OLCI bands are optimized for measuring ocean colour in the coastal zones (Donlon et al., 2012).

The Sentinel-3 satellites are in a sun-synchronous orbit with the OLCI tilted 12.6° westwards, mitigating the sunglint contamination (Donlon et al., 2012). With the two-satellite configuration, the average revisit time at the equator is less than 1.9 days and less than 1.4 days for latitudes larger than 30° , i.e. the Kattegat Sea (Donlon et al., 2012). The OLCI has a swath width of 1270 km and delivers data with the ground spectral resolution of 300 meters (Donlon et al., 2012). The spectral bands are a heritage from MERIS, with 6 additional bands for increased atmospheric correction (Oa1, Oa14-Oa15 and Oa20-Oa21) and an improved Chl-a fluorescence measurement (Oa9) (Tab. 1) (Donlon et al., 2012; EUMETSAT, 2018; Kyryliuk, 2019).

1.2.2 Processing Levels and Data Products

The raw data from the OLCI is processed on three levels. The level 0 (L0) processing includes annotation and time sorting of the raw sensor data (EUMETSAT, 2018). The level 1 (L1) processing converts the L0 data to geo-located TOA radiance for each of the 21 OLCI wavelength bands (Tab. 1). The level 2 (L2) processing applies two different ACs on the L1 data, the Baseline AC (BAC) for Case-1 waters and the Alternative AC (AAC) for Case-2 waters, resulting in L_w . The L_w is then used for retrieving concentrations and IOPs for the in-water constituents through algorithm processors run in parallel. The Ocean Colour for MERIS (OC4Me) algorithm, fed by the BAC, retrieves the Chl-a concentration in Case-1 waters and the Case-2 Regional CoastColour (C2RCC) algorithm, fed by the AAC, retrieves the concentrations for Chl-a and TSM, as well as the absorption coefficient for

coloured detritus and dissolved matter at 443 nm (ADG443), in Case-2 waters ([EUMETSAT, 2018](#)).

Within the L2 processing, the $L_w(\lambda)$ is also normalized, approximating the sun position at zenith, absence of atmosphere and a mean distance between Sun and Earth, according to

$$L_{wn}(\lambda) = \frac{L_w(\lambda)}{t_{down}(\lambda)\mu_s C_s} \quad (15)$$

where L_{wn} is the normalized L_w , λ is the wavelength, t_{down} is the downward transmittance of the atmosphere, μ_s is the cosine of the solar zenith angle, and C_s is a coefficient accounting for the variation in the Sun-Earth distance ([EUMETSAT, 2018](#)). Furthermore, the conversation to remote sensing reflectance $R_{rs}(\lambda)$ is through

$$R_{rs}(\lambda) = \frac{L_{wn}(\lambda)}{F_0(\lambda)} \quad (16)$$

where F_0 is the mean solar spectral irradiance at the top of the atmosphere ([EUMETSAT, 2018](#)). Note that $F_0(\lambda)$ is the same as the atmospherically corrected $E_d(0^+, \lambda)$ in equation 11 ([EUMETSAT, 2018](#); [Morrow et al., 2010](#)). The $R_{rs}(\lambda)$ is then multiplied with the sun at zenith (π), resulting in the unit-less water-leaving reflectance $\rho_w(\lambda)$ (Eq. 17) ([EUMETSAT, 2018](#)).

$$\rho_w(\lambda) = \pi R_{rs}(\lambda) \quad (17)$$

The angular dependent ρ_w is calculated for 16 OLCI bands (Tab. 1). The remaining 5 bands (Oa13-15 and Oa19-20) are excluded since they are dedicated to atmospheric gas absorption measurements and AC ([EUMETSAT, 2018](#)).

Every processing level, except L0, outputs a data product publicly available. The L1 and L2 end products are publicly available for download through the [Copernicus Online Data Access \(CODA\)](#) service for one year after sensing date, and thereafter they are reprocessed and available at [CODA reprocessed \(CODAREP\)](#). The OLCI data products are distributed from sensing date 26 April 2016 onward. The data come in full resolution, 300x300 meter pixels, and reduced resolution, 1200x1200 meter pixels. They are available in near real-time (NRT) and non-time critical (NTC) products, delivered in less than 3 hours and one month after acquisition, respectively. The NRT product uses modeled meteorological variables and the NTC product uses collected meteorological data, both from the European Centre for Medium-

Range Weather Forecasts (ECMWF) (EUMETSAT, 2018). Therefore, the full resolution, NTC L2 product is most applicable for ocean colour and water quality studies.

In addition, the L2 data comes with a number of quality and classification flags, some inherited from the previous processing levels (EUMETSAT, 2018). These flags can be used in combination for masking out the land and bad pixels, i.e. clouds, missing data, and algorithms failures.

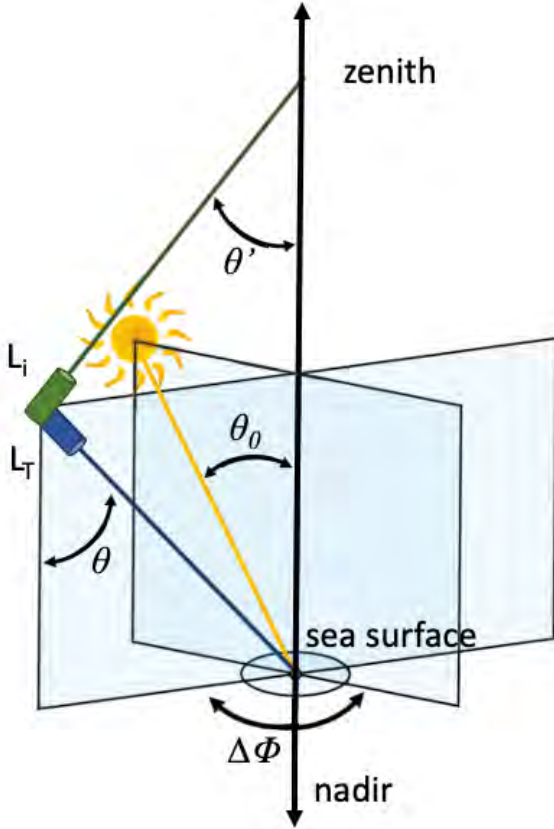


Figure 5: Definition of the sun zenith angle (θ_0) and the measurement geometry related to in situ above-water radiance measurements. The sensor (blue) measuring the total radiance emerging from the sea surface (L_T) has nadir angle $\theta=40^\circ$ and the sensor (green) measuring the sky radiance (L_i) has the same zenith angle $\theta'=40^\circ$. Both sensors are in the same plane with the difference between the sun and sensor azimuth angle $\Delta\Phi=135^\circ$, pointing away from the sun. Based on Li et al. (2019) and Morel et al. (2002).

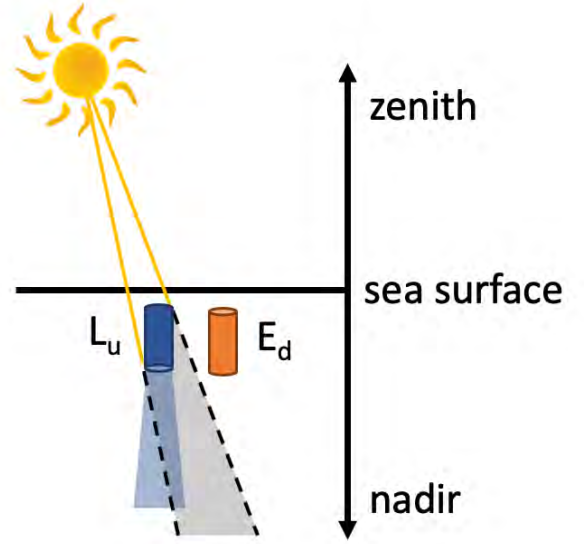


Figure 6: Subsurface sensors of the in situ in-water system with the sensor (blue) measuring the upwelling radiance (L_u) pointed at nadir and the sensor (orange) measuring the downwelling irradiance (E_d) pointed at zenith. The shadow cast by the sensor housing (gray area) affects the radiance measurement where it overlaps with the sensor field-of-view (blue area). The effect is called self-shading and must be corrected for.

1.3 In Situ Radiometric Measurements

The water-leaving reflectance $\rho_w(\lambda)$ calculated from satellite measurements can also be retrieved from radiometric measurements in situ (Eq. 11). Both in-water and above-water methods are used for the optical measurements (Zibordi et al., 2012). The majority of the radiometric data found in databases used for developing global bio-optical algorithms are from in-water measurements (O'Reilly, 2000). Although, there is no proven reason for choosing one method over the other, this may be because in-water methods have been used for a longer time and because of the historical discrepancy between the methods, where the in-water system has been preferred (Hooker et al., 2004). For both methods, $L_w(\lambda)$ cannot be measured directly because of wave perturbations and must be derived (Kleiv et al., 2015).

Above-water systems are based on measurements of the total radiance emerging from the sea surface $L_T(\theta, \Delta\Phi)$, the sky radiance $L_i(\theta', \Delta\Phi)$ and E_d (Zibordi et al., 2012). The angle from nadir (θ), the angle from zenith (θ') and the difference between the sun and sensor azimuth angle ($\Delta\Phi$) defines the measurement geometry (Fig. 5). The $L_T(\theta, \Delta\Phi)$ sensor is pointed at the sea surface with nadir angle $\theta=40^\circ$, avoiding sunglint (path D in Fig. 4), and the $L_i(\theta', \Delta\Phi)$ sensor is pointed at the sky with zenith angle $\theta'=40^\circ$, avoiding sky glint (path B in Fig. 4) (Hooker et al., 2004; Zibordi et al., 2012). Both sensors are in the same plane, pointed away from the sun, with azimuth angle $\Delta\Phi=135^\circ$ (Mobley, 1999). From these measurements $L_w(\theta, \Delta\Phi, \lambda)$ is calculated according to

$$L_w(\theta, \Delta\Phi, \lambda) = L_T(\theta, \Delta\Phi, \lambda) - \rho(\theta, \Delta\Phi, \theta_0, W) L_i(\theta', \Delta\Phi, \lambda) \quad (18)$$

where ρ is the sea surface reflectance determined from the measurement geometry, the sun zenith angle θ_0 , and the sea state estimated by wind speed W (Zibordi et al., 2012). $L_w(\lambda)$ at nadir-view is then retrieved according to

$$L_w(\lambda) = L_w(\theta, \Delta\Phi, \lambda) \frac{\Re_0}{\Re(\theta, W)} \frac{Q(\theta, \Delta\Phi, \theta_0, \lambda, \tau_a, IOP)}{Q_n(\theta_0, \lambda, \tau_a, IOP)} \quad (19)$$

where \Re_0 (i.e. $\Re(\theta, W)$ at $\theta=0^\circ$) and $\Re(\theta, W)$ account for the sea surface reflectance and refraction and Q and Q_n denote the Q-factors which describe the anisotropy (dependency of direction) of the in-water radiance at angle θ and at nadir (i.e. $\theta=0^\circ$), respectively (Zibordi et al., 2012). The Q-factors also depend on $\Delta\Phi$ and θ_0 , the optical properties of the atmosphere, estimated by the aerosol optical thickness (τ_a), and the IOPs (Zibordi et al., 2012). The

factors have been theoretically determined describing different conditions and are available in look-up tables (Mobley, 1999; Morel et al., 2002). Then, $R_{rs}(\lambda)$ and $\rho_w(\lambda)$ are determined according to equation 11 and 17.

In-water systems follows the method established by Smith and Baker (1984). The subsurface upwelling radiance $L_u(z, \lambda, t)$ and $E_d(z, \lambda, t)$ or upwelling irradiance $E_u(z, \lambda, t)$ are measured at depth z , wavelength λ and, time t , either at fixed depths or as continuous profiles (Morrow et al., 2010; Zibordi et al., 2012). The sensors detecting upwelling light are pointed at nadir and for detecting downwelling light the sensors are pointed at zenith (Fig. 6). The above-water $E_d(0^+, \lambda, t)$ is also monitored simultaneously and used for removing the perturbations related to illumination change, performed as

$$\mathfrak{P}(z, \lambda, t_0) = \mathfrak{P}(z, \lambda, t) \frac{E_d(0^+, \lambda, t_0)}{E_d(0^+, \lambda, t)} \quad (20)$$

where $\mathfrak{P}(z, \lambda, t_0)$ is the radiometric parameters (L_u , E_d or E_u) as if they were measured at all z depths at time t_0 (Morrow et al., 2010; Zibordi et al., 2012). t_0 is generally chosen to coincide with the start of the acquisition sequence (Morrow et al., 2010). The $\ln[\mathfrak{P}(z, \lambda, t_0)]$ is evaluated against z within the extrapolation interval $z_1 < z < z_2$ through least-square linear regression, computing the $\mathfrak{P}(0^-, \lambda, t_0)$ determined as the exponential of the intercept (Morrow et al., 2010). 0^- denotes the depth just below the sea surface and the extrapolation interval is the near-surface layer where the requirement of linear decay of $\mathfrak{P}(z, \lambda, t_0)$ with depth is satisfied (Zibordi et al., 2012). The negative slopes of the regression fits are the diffuse attenuation coefficients $K_{\mathfrak{P}}(\lambda)$, i.e $K_l(\lambda)$, $K_d(\lambda)$ and $K_u(\lambda)$ calculated from $L_u(z, \lambda, t_0)$, $E_d(z, \lambda, t_0)$ and $E_u(z, \lambda, t_0)$ respectively, within the chosen extrapolation interval (Zibordi et al., 2012). Omitting the t_0 , the $L_w(\lambda)$ is calculated from the $L_u(0^-, \lambda)$ propagated through the sea surface, according to

$$L_w(\lambda) = 0.54 L_u(0^-, \lambda) \quad (21)$$

where 0.54 accurately accounts for the upwelling radiance reduction from reflectance and transmission across the sea-air interface (Mobley, 1999). However, because the $L_u(z, \lambda)$ sensor is directed downwards the measurement is unavoidably affected by the shadow cast by the sensor housing, an error called self-shading (Fig. 6), which must be corrected for (Shang et al., 2017). Direct comparison between the extrapolated $E_d(0^-, \lambda)$ and the independently

measured above-water $E_d(0^+, \lambda)$, which should closely agree, reveals the poor quality data acquisitions (Morrow et al., 2010). Then, $R_{rs}(\lambda)$ and $\rho_w(\lambda)$ are determined according to equation 11 and 17.

1.3.1 In-Water Spectral Corrections

The reduction of upwelling radiance (L_u) caused by the sensor housing shadow is described by the relative self-shading error (ϵ) according to

$$\epsilon = \frac{L_u^{true} - L_u^{measured}}{L_u^{true}} \quad (22)$$

where L_u^{true} and $L_u^{measured}$ is the upwelling radiance without shading and with shading, respectively (Gordon and Ding, 1992). According to Gordon and Ding (1992), the self-shading is estimated by the subsurface solar zenith angle, the absorption coefficient of the medium, the ratio between diffuse and direct sun irradiance, and the housing radius (Shang et al., 2017; Zibordi and Ferrari, 1995). However, the self-shading was also estimated by Aas and Korsbø (1997) in the coastal waters of the outer Oslofjord for sun zenith angles $\theta_0=40-60^\circ$ to

$$\ln(1 - \epsilon) = \ln\left(\frac{L_u^{measured}}{L_u^{true}}\right) = -BK_l r \quad (23)$$

where B is a function of wavelength and θ_0 determined from linear least-square regression between r and $L_u^{measured}$, the K_l is the diffuse attenuation coefficient of upwelling radiance, and r is the housing radius. The self-shading correction factor $f(\lambda)$ was then determined from equation 23 as

$$f(\lambda) = \frac{L_u^{true}}{L_u^{measured}} = e^{BK_l r} \quad (24)$$

for correction of $L_u^{measured}$, retrieving the L_u^{true} (Aas and Korsbø, 1997; Kleiv et al., 2015). The self-shading error estimates from equation 23 differed by less than 7% from the method suggested by Gordon and Ding (1992) (Aas and Korsbø, 1997).

When sensors calibrated in air are submerged into water the absolute response changes because of the different refraction indices of the two media (Zibordi et al., 2004). The radiance immersion correction factor $F_i(\lambda)$ is determined by

$$F_i(\lambda) = \left(\frac{n_g(\lambda) + n_w(\lambda)}{n_g(\lambda) + 1}\right)^2 n_w \quad (25)$$

where $n_g(\lambda)$ is the refractive index of the window and $n_w(\lambda)$ is the refractive index of seawater, determined according to

$$n_w(\lambda) = 1.325147 + \frac{6.6096}{\lambda - 137.1924} \quad (26)$$

(Ohde, 2003). However, the immersion factors for irradiance sensors must be determined empirically.

1.4 Requirements for the OpenSpecRad

The in situ Open-source SpectroRadiometer (OpenSpecRad) system should be able to retrieve $\rho_w(\lambda)$ according to the in-water method. The specific angle-dependent measurement geometry in the above-water method is complex and therefore hard to satisfy for a simple self-built system. With the help of gravity, it is easier to achieve the vertical positions needed for the in-water method. The in-water method will also provide data with vertical resolution.

The sensors for $E_d(z, \lambda)$ and $L_u(z, \lambda)$ on the in-water instrument, as well as the above-water sensor for $E_d(0^+, \lambda)$ must meet the requirement of vertical positions. For in-water measurements, this had previously been solved with a wing and bottom weight in the optical profiler HyperPro II (Sea-Bird Scientific) design (Fig. 7). Commercial optical profilers, as the HyperPro II, cost around 800 000 to 1 million Swedish crowns. The OpenSpecRad should be affordable.



Figure 7: The optical profiler HyperPro II (Sea-Bird Scientific) which the Open-source SpectroRadiometer (OpenSpecRad) in-water instrument design was inspired by. When sinking through the water column the frame wing and bottom weight keep the $E_d(z, \lambda)$ (the cylinder furthest away) and $L_u(z, \lambda)$ (the cylinder closest) vertical. From Sea-Bird Scientific (2017).

The spectrometers (when calibrated, called spectroradiometers) must be small and sensitive to

the low light condition underwater. The STS-VIS miniature spectrometer (size 42x40x24 mm, spectral range 350-800 nm) have frequently been used in self-built spectral sensors both above and underwater, e.g. in unmanned aerial vehicles (UAVs) for characterization of terrestrial vegetation (Burkart et al., 2014) and submerged aquatic vegetation (Brooks et al., 2019), cyanobacteria blooms (Becker et al., 2019; Boddula et al., 2017) and Chl-a monitoring from above water (Grósz et al., 2019), and downwelling underwater light for benthic mapping (Bongiorno, 2014). The spectrometer was coupled to a micro-controller (Burkart et al., 2014) or the single-board computer Raspberry Pi (RPI) (Becker et al., 2019; Boddula et al., 2017; Brooks et al., 2019), powered by a battery.

The underwater housings should at least withstand the pressure at 50 meters depth for safe usage to 20-25 meters. A cylindrical shaped container is more pressure-proof than a rectangular-shaped and is compatible with a threaded lid. The manufacturing must be relatively cheap and fast, therefore 3D-printing is a good option. Common thermoplastics used in 3D-printing are acrylonitrile butadiene styrene (ABS), polylactic acid (PLA), nylon, and composites of plastics and continuous or chopped fibers (Champion et al., 2016). However, both PLA and nylon absorb water which makes the material weaker over time.

The spectrometers must be put behind a pressure window, which should have excellent transmission properties ($<95\%$) over the spectral wavelength range. Common materials for pressure windows are acrylic, quartz glass, and crown glass. Bongiorno (2014) used a 4 mm thick plane quartz glass for submersion down to 20-30 meters depth. Although, dome-shaped windows are stronger than plane glass under pressure.

1.5 Bio-optical Algorithms

Empirical bio-optical band-ratio algorithms are established through statistical regression between coincident in situ measurements of in-water constituents and radiometric observations of the water-leaving radiance (ρ_w) (Ogashawara, 2015). Inputs from satellite or in situ radiometric measurements are ρ_w or R_{rs} of at least two different wavelength bands and the output is the concentration of Chl-a, CDOM, or TSM. The bands are expressed as a band-ratio since the uncertainties related to light propagation through the sea-air interface cancel out ($t_{down}(\lambda)$, μ_s , and C_s in Eq. 15) (Seelye, 2014). When OLCI bands are used in

CDOM band-ratios algorithms, the CDOM detection limit primarily depends on the OLCI sensitivity of the TOA radiance and the accuracy of atmospheric correction applied in the processing, however this has yet not been quantified.

The general form CDOM band-ratio algorithm evaluated in this study have previously been evaluated, after fitting, for prediction of CDOM in the Baltic Sea (Tab. 2) (Ligi et al., 2017; Toming et al., 2017). Starting from the general form, the slope and intercept are calculated for predicting the concentration of the in-water constituents for the local area (Ligi et al., 2017).

Table 2: The previously published CDOM band-ratios evaluated in this study, with the water-leaving reflectance (ρ_w) algorithm wavelengths and the corresponding Sentinel-3 Ocean and Land Colour Instrument (OLCI) band-ratios closest to the algorithm center wavelengths.

General form	OLCI bands	Code	Reference
450-515/750-900	Oa5/Oa16	CDOM1	Brezonik et al. (2005)
665/490	Oa8/Oa4	CDOM2	Koponen et al. (2007)
400/600	Oa1/Oa7	CDOM3	Doxaran et al. (2005)
530-610/630-690	Oa6/Oa8	CDOM4	Kallio et al. (2008)
664/550	Oa8/Oa6	CDOM5	Ammenberg et al. (2002)
670/571	Oa9/Oa6	CDOM6	Menken et al. (2006)
490/550	Oa4/Oa6	CDOM7	Kowalczyk et al. (2005)
665/754	Oa8/Oa12	CDOM8	Koponen et al. (2007)
674/754	Oa9/Oa12	CDOM9	Kutser et al. (2005)

1.6 Validation Statistics

The ability of the band-ratio algorithms for predicting the in situ $a_{CDOM}(443)$ is evaluated by mean normalized bias (MNB), root mean square error (RMSE), and absolute percentage difference (APD) (Eq. 27-29) (Kiryliuk and Kratzer, 2019; Ligi et al., 2017). MNB evaluates the off-set from 1:1 line, RMSE evaluates the scatter, and APD evaluates the error (Kiryliuk and Kratzer, 2019).

$$MNB (\%) = \frac{1}{N} \sum_{i=1}^N \left(\frac{Calculated_i - Reference_i}{Reference_i} \right) \times 100 \quad (27)$$

$$RMSE (\%) = \sqrt{\frac{1}{N} \sum_{i=1}^N \left(\frac{Calculated_i - Reference_i}{Reference_i} \right)^2} \times 100 \quad (28)$$

$$APD (\%) = \exp \left(\text{mean} \left| \ln \left(\frac{Calculated_i - Reference_i}{Reference_i} \right) \right| \right) - 1 \times 100 \quad (29)$$

where N is the sample size, *Calculated* is the $a_{CDOM}(443)$ predicted by the fitted band-ratio algorithms and *Reference* is the measured in situ $a_{CDOM}(443)$.

2 Materials and Method

2.1 Bio-optical Algorithms

2.1.1 Fitting

The Sentinel-3 OLCI bands corresponding to the CDOM band-ratio algorithms were fitted by linear least-squares regression for predicting the in situ $a_{CDOM}(443)$ in the Kattegat (Tab. 2), using MATLAB (R2017b). The samples were collected at 5 meters depth during a cruise with R/V Skagerrak on 24-27 April 2019 (Fig. 8). The in situ $a_{CDOM}(443)$ was calculated according to equation 10 at wavelength 443 nm from absorbance measurements (Aqualog-UV-800, HORIBA Scientific). The 1x1 pixels corresponding to the sampling stations were extracted from the OLCI data (NTC L2, full resolution) closest in time and space. The average time difference between the in situ sampling and the satellite data was 2 days, 15 hours, and 47 minutes (standard deviation, $s=10$ hours). A non-valid-pixel expression was evaluated and applied to the pixels, including the following flags; land, cloud, cloud-ambiguous, cloud-margin, invalid, cosmetic, saturated, suspect, hisolzen, highglint, AC-fail, and whitecaps. 20 out of 23 stations had valid pixels and were used in the fitting.

2.1.2 Validation

The validation of the locally fitted bio-optical algorithms was conducted by correlation analysis between in situ reference measurements and satellite-derived $a_{CDOM}(443)$. Each algorithm was applied to the OLCI data (NTC L2, full resolution, 1x1 pixels) closest in time and space to the in situ measurements. The OLCI L2 C2RCC product ADG443 (1x1 pixels) were also included in the analysis. The in situ CDOM was measured by the Norwegian Institute for Water Research (NIVA) FerryBox onboard the M/S Color Fantasy (Color Line), traveling between Oslo, Norway and Kiel, Germany (Fig. 8). The FerryBox measured the CDOM

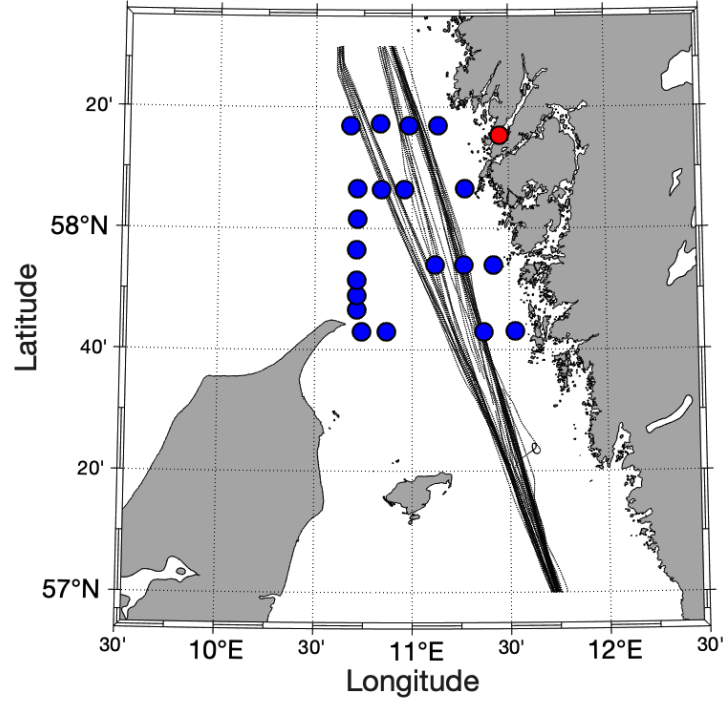


Figure 8: Sample stations for all in situ data used in this study, with blue dots where $a_{CDOM}(443)$ data for fitting the band-ratio algorithms was collected, red dot where the radiometric measurement using the Open-SpecRad took place, and small black dots where Ferrybox data were collected for validation of the local algorithms.

fluorescence (TriOS GmbH MicroFlu) at 4 meters depth and NIVA performed a conversion to $a_{CDOM}(443)$ from local relationships between CDOM fluorescence and absorbance. However, during some periods the fluorometer had condensation on the sensor window, resulting in false negatives. For detecting these data, the inverse relationship between salinity and $a_{CDOM}(443)$ was investigated and outliers were removed, resulting in 235 days of data between May 2016 and August 2018. Only 43 of these had relatively cloud-free conditions on the OLCI satellite image from the corresponding day. The non-valid-pixel expression was applied onto the OLCI bands and the same expression, except AC-fail and whitecaps and including OCNN-fail, was used on the ADG443 product. 9481 and 9304 in situ measurements were used for validation of algorithms and the ADG443 product, respectively. The average time difference between the in situ and satellite data was 10 hours ($s=2.5$ hours). The validation was evaluated using equations 27-29.

2.2 OpenSpecRad Development

The in situ Open-source SpectroRadiometer (OpenSpecRad) system was developed for measuring the downwelling irradiance $E_d(z, \lambda)$ and upwelling radiance $L_u(z, \lambda)$ using an in-water instrument (Fig. 1), as well as the downwelling irradiance just above the sea surface $E_d(0^+, \lambda)$ using a separate unit (Fig. 17, Appendix A). The building process is described in Appendix A.

2.2.1 Performance Testing

The pressure and water-resistance of the housings and glass domes were tested by lowering down the in-water instrument to 50 meters depth with the $E_d(z, \lambda)$ and $L_u(z, \lambda)$ units replaced by ballast weights. A camera mounted beside the bottom weights, angled towards the housings, filmed the lowering for evaluation of the instrument tilt.

The dome interference was evaluated by measuring the intensity of a halogen lamp put in one end of a 70 cm paper tube and the $E_d(z, \lambda)$ unit put in the other end, with and without the dome.



Figure 9: The radiance sensor with barrel attached, behind the dome inside the housing.



Figure 10: The irradiance sensor with the large area cosine corrector attached, behind the dome inside the housing.

2.2.2 Spectroradiometer Calibrations

The calibration of absolute radiance was performed using a halogen calibration light source (DH-2000-CAL, Ocean Optics). A dark measurement was recorded by covering the $L_u(z, \lambda)$ spectrometer barrel (Fig. 9) with a dark cloth. After letting the light source warm-up for 20

minutes, the spectrometer was attached to the source and 5 measurements were recorded and averaged. The dark subtracted measurement was divided by the integration time and light collection area. The calibration file for the light source was used to calculate the calibration vector, according to

$$\text{Calibration vector } [\mu\text{J}/\text{DC}/\text{nm}] = \frac{\text{Calibration file } [\mu\text{J}/\text{s}/\text{cm}^2/\text{nm}]}{\text{Dark subtracted measurement } [\text{DC}/\text{s}/\text{cm}^2]} \quad (30)$$

where the J is joule, DC is digital count, nm is nanometer, cm^2 is cubic centimeter and s is second. The calibration vector was further divided by the solid angle of the radiance sensor, calculated according to equation 5 with the spherical surface area $A = 2\pi r^2(1 - \cos 12.5^\circ)$ using the half-angle field-of-view of 12.5° .

Since the cosine correctors (CC-3-DA Spectralon diffuser, Ocean Optics) on the irradiance spectrometers $E_d(z, \lambda)$ and $E_d(0^+, \lambda)$ did not fit the halogen calibration light source (Fig. 10), a calibration file was created for another halogen lamp (20 W, 12 V). The lamp was attached in one end of a 70 cm paper tube and its absolute irradiance was measured with a spectrometer using a smaller area cosine corrector (CC-3-UV-S Spectralon diffuser, Ocean Optics) attached via an optic fiber, which previously was calibrated with the halogen calibration light source for irradiance (Eq. 30). The calibration of absolute irradiance with the larger area cosine correctors (CC-3-DA) attached was then performed according to equation 30, using the halogen lamp. The calibration was performed for both irradiance spectrometers.

2.3 OpenSpecRad Measurement and CDOM Analysis

A radiometric measurement was performed with the OpenSpecRad outside Kristineberg, Fiskebäckskil (Fig. 8) on 22 July 2020 between 14:16-14:24 with solar zenith angle $\theta_0=41.07-41.63^\circ$. The above-water unit was directed straight up and fastened onto the highest point of the boat, avoiding any shadows. The in-water instrument was deployed on the sunny side of the boat, with the L_u housing positioned furthest from the boat, avoiding the boat shadow and reducing self-shading. The measurement was started from a laptop. The $E_d(0^+, \lambda)$, $E_d(z, \lambda)$ and $L_u(z, \lambda)$ were collected simultaneously with integration times 1, 2, and 10 seconds, respectively, averaging three recordings at wavelengths 350-800 nm. The $E_d(0^+, \lambda)$ was measured every 18 seconds, resulting in 25 measurements during the 7.5 minutes. The in-water instrument parameters were recorded every 0.5 ± 0.2 meters between 0.5-20 meters

depth. Dark current measurements were recorded each for the radiometric parameters by covering the dome/collection area with a black cloth.

Water samples were collected in 250 mL bottles at the depths corresponding to the radiometric measurement. Each bottle was rinsed three times with sample water before collecting the sample. The samples were filtered through 0.45 μm filters (Whatman, GMF w/GMF) and stored cold and dark until analysis. The absorbance was measured (Aqualog-UV-800, HORIBA Scientific) at wavelengths 350-800 nm with integration time 10 seconds, 3 nm increment, and medium CCD gain. The samples were room tempered at analysis.

2.3.1 Spectral Processing and Bio-optical Algorithm Validation

The dark current was subtracted from the corresponding radiometric measurements. The in-water measurements were corrected for illumination change during the acquisition according to equation 20, with t_0 chosen at the start of the measurement. The $\ln[E_d(z, \lambda, t_0)]$ and $\ln[L_u(z, \lambda, t_0)]$ were evaluated against extrapolation depths $1 < z < 3$ and $0.5 < z < 4$ meters, respectively, through linear least-square regression. The $\ln[E_d(0.5, \lambda, t_0)]$ was excluded since it did not fulfill the requirement of linear decay with depth. The $E_d(0^-, \lambda, t_0)$ and $L_u(0^-, \lambda, t_0)$ were each computed as the exponential of the intercept. $E_d(0^-, \lambda, t_0)$ was compared to $E_d(0^+, \lambda, t_0)$.

$L_u(0^-, \lambda, t_0)$ was corrected for self-shading according to equation 24, using sensor radius 2.5 centimeter. The immersion factor $F_i(\lambda)$ was applied with n_g interpolated from the dome glass technical information for a 10 mm thick window (Knight Optical, 2020), resulting in $L_u^{true}(0^-, \lambda, t_0)$ (Eq. 25). The $L_w(0^+, \lambda, t_0)$ was determined from the $L_u^{true}(0^-, \lambda, t_0)$ (Eq. 21). The $R_{rs}(\lambda)$ was then computed through equation 11. To match the OLCI bands the $R_{rs}(\lambda)$ spectra was re-sampled by averaging over the corresponding band wavelengths (Tab. 1). The water-leaving reflectance $\rho_w(\lambda)$ was calculated from re-sampled $R_{rs}(\lambda)$ according to equation 17.

From the absorbance measurements of water samples, the CDOM absorption coefficient $a_{CDOM}(443)$ was calculated at wavelength 443 nm (Eq. 10). The fitted band-ratio algorithms were applied on the $\rho_w(\lambda)$ and evaluated against the $a_{CDOM}(443)$ from the sample at 4 meters depth.

The derived $\rho_w(\lambda)$ was also compared to the corresponding bands from Sentinel-3 OLCI satellite data (NTC L2, full resolution) sensed on 22 July 2020 between 10:04-10:07. The 1x1 pixels corresponding to the sampling station were extracted from the OLCI data. The non-valid-pixel expression was applied for removing bad pixels.

3 Result and Discussion

3.1 Sentinel-3 OLCI: Bio-optical Algorithm Validation

The regression fits of the general form band-ratio algorithms for predicting $a_{CDOM}(443)$ is presented in table 3. None of the fits showed a good result, with the highest $R^2=0.25$ for algorithm CDOM2. A high R^2 is important for the ability of the model to precisely predict a value. Although not the scope of this study, all possible combinations of band-ratios were tested for finding a better fit. The Oa10/Oa09 produced the best fit, $R^2=0.56$, however not satisfying. This is probably due to the large mean time difference of 2.25 days between the in situ measurements and the cloud-free OLCI satellite images. The cloud-coverage is clearly a weakness for satellite remote sensing over the Kattegat. The problem of extensive cloud cover was also seen in the validation of the fitted algorithms, where only 18% of the days with available Ferrybox measurements could be matched with satellite data from the same day.

Most satellite validation protocols require a maximum of 2-3 hours difference between in situ and satellite measurements (Kutser et al., 2018). Although, it is not always possible to fulfill, especially for Ferrybox data because ferries often travel by night. It is a trade-off between sample size and minimizing time difference, therefore some validation studies use data with 8-24 hours difference (Kowalczyk et al., 2010; Kutser et al., 2018; Mannino et al., 2014). The 10 hour mean average time difference between the in situ Ferrybox data used in this study should be sufficient for proper validation.

However, the bad regression fits reflect the results of the validation of the algorithms (Tab. 3). None of the CDOM algorithms showed correlation with the in situ $a_{CDOM}(443)$. The validation statistics, with very large RMSE and APD, confirm that there are much scatter and overall error in the validation. Neither the L2 OLCI C2RCC product for coloured detritus

Table 3: The fitted CDOM band-ratio algorithms and the validation statistics, with * marking significance ($p < 0.05$), MNB is the mean normalized bias, RMSE is the root mean square error and APD is the absolute percentage difference (Eq. 27-29). N=9481, N=9481 and N=9304 for CDOM1-9, Oa10/Oa09 and ADG443, respectively.

Fitted algorithm	Code	R ²	MNB(%)	RMSE(%)	APD(%)
$0.0006 \times \text{Oa5}/\text{Oa16} + 0.3772$	CDOM1	0.0088	38	3669	341
$-3.7946 \times \text{Oa8}/\text{Oa4} + 1.0126$	CDOM2	0.0203*	118	11495	206
$0.0402 \times \text{Oa1}/\text{Oa7} + 0.3027$	CDOM3	0.0087	33	3193	611
$-0.0392 \times \text{Oa6}/\text{Oa8} + 0.5828$	CDOM4	0.0017	-7	724	899
$-3.0501 \times \text{Oa8}/\text{Oa6} + 0.9573$	CDOM5	0.0356*	160	15615	132
$-3.1444 \times \text{Oa9}/\text{Oa6} + 0.9533$	CDOM6	0.0354*	132	12858	173
$0.2187 \times \text{Oa4}/\text{Oa6} + 0.1437$	CDOM7	-0.0940*	27	2637	587
$0.0029 \times \text{Oa8}/\text{Oa12} + 0.3807$	CDOM8	-0.0306*	34	3309	360
$0.0026 \times \text{Oa9}/\text{Oa12} + 0.3810$	CDOM9	-0.0265*	35	3361	354
	ADG443	0.0213*	-67	6426	2245
$0.8596 \times \text{Oa10}/\text{Oa09} - 0.5109$		-0.0127	-14	1345	582

and dissolved matter, ADG443, nor the best fit Oa10/Oa09 showed any correlation with the in situ measurements. In contrast, the ADG443 showed a good correlation with $a_{CDOM}(440)$ ($R^2=0.8$, MNB 8%, RMSE 56%, APD 54%, N=18) and even better than an OLCI C2RCC product excluding detritus in the Baltic Sea (Kyryliuk and Kratzer, 2019). For the Kattegat, the coloured detritus included in the ADG443 may contribute to the uncorrelation. Blix et al. (2018) found that the correlation between the OLCI C2RCC products and in situ measurements was low and not significant in Lake Balaton, Hungary. Although the Baltic Sea and lake water are distinctly different from the Kattegat, the results show that the OLCI ADG443 product has problems and should not be used for prediction of $a_{CDOM}(443)$ in the Kattegat.

3.2 Usage and Performance of the OpenSpecRad

The Open-source SpectroRadiometer (OpenSpecRad) system development resulted in an in-water instrument (Fig. 1), measuring the vertical profile of downwelling irradiance $E_d(z, \lambda)$ and upwelling radiance $L_u(z, \lambda)$ and an above-water downwelling irradiance $E_d(0^+, \lambda)$ sensor unit (Fig. 17, Appendix A). Each unit is turned on/off by attaching/detaching the battery. After start-up, the system is operated by connecting a laptop to the Wi-Fi network managed

by the above-water unit. The measurement is started from the laptop shell and the three radiometric parameters are measured simultaneously. The in-water instrument can operate down to 20 meters depth. After the measurement is finished the collected data is transferred wirelessly to the laptop. Only two people are needed to perform a measurement. The total cost was around 10% of a commercial optical profiler. Drawings for printing and building the OpenSpecRad system are open-source and available at [GitHub](#).

The pressure and water resistance tests of the housings and domes were successful. The housings withstood the water pressure at 50 meters depth while keeping the inside dry. When the in-water instrument was lowered down it was stable and vertical all the way down. However, if accelerometers for pitch and roll were added to one of the units small tilts could be accurately measured and corrected for. Even small tilts can affect the accuracy of the radiometric measurements and may have introduced errors in data.

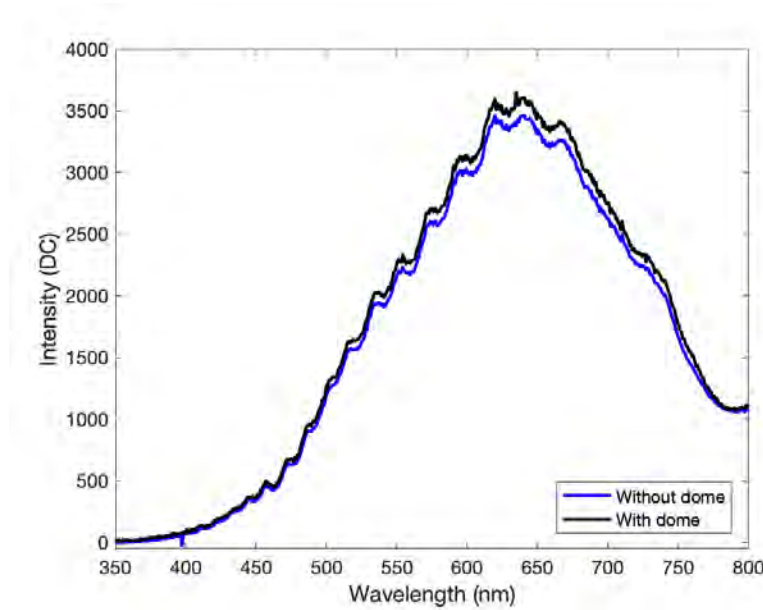


Figure 11: Dark subtracted spectra of measurement of the halogen lamp without and without the dome.

The dome characterization showed that the signal increased when measuring through the dome (Fig. 11). It was not expected since the transmission for 10 mm thick dome glass was 96.7-99.8% over wavelengths 350-800 nm ([Knight Optical, 2020](#)). The increase was the largest between 500-760 nm (Fig. 12). This may be caused by the shape of the dome or fluctuating intensity emitted by the halogen lamp. Any correction for the dome was not added, since the irradiance calibration introduced a much larger error.

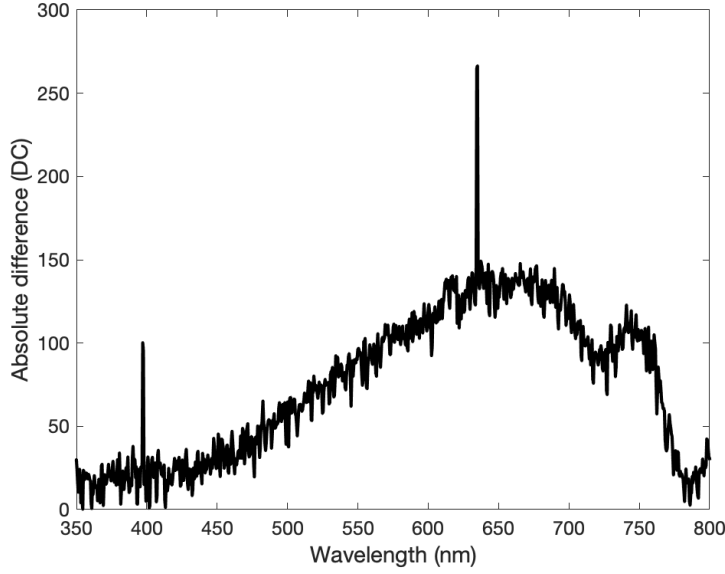


Figure 12: Absolute difference of intensity between measurement of the halogen lamp without and with the dome.

The halogen calibration light source available was only compatible with the radiance spectroradiometer barrel and the small area cosine corrector. Therefore, an accurate radiance calibration was chosen instead of doing the calibration through the dome with the halogen lamp. Although, some error was introduced when the solid angle was calculated for air and not for water, because the angle decreases when submerged. The small area cosine corrector was used for transferring the calibration to an ordinary halogen lamp for irradiance calibration of the large area cosine correctors. However, the halogen lamp had too low intensity between 350-400 nm and 725-800 nm for good calibration. For proper calibration, a calibration light source that fitted the large area cosine correctors should have been used, alternatively, the spectrometer could have been sent to the calibration service at the manufacturer.

Regardless, when performing a calibration the set-up should be as close to the measurement set-up as possible. The best option would be to use a stable calibration light over 350-800 nm for calibration of the spectrometers mounted inside the housings behind the domes. Thereby the transmission properties of the dome would also be compensated for. The limited calibration used here introduces error which propagates to the derived $\rho(\lambda)$.

3.3 OpenSpecRad: Bio-optical Algorithm Validation

The in situ measurement with OpenSpecRad only resulted in $E_d(z, \lambda)$ and $L_u(z, \lambda)$ recordings at 0.5-3 and 0.5-4 meters, respectively, instead of a continuous vertical profile until 20 meters depth. This was caused by the measurement acquisition ending after 100 retries to reach the requested depth. The in-water instrument was probably lowered down too fast, missing the requested depth. This may be avoided if the measurements were triggered by time and not by depth. The lowering was also disrupted by the waves, occasionally pulling the instrument up and down. The total weight of the instrument could also be changed or a buoyancy chamber added for adjusting the sinking rate, making it a free-falling profiler. However, the wireless communication between the laptop, the in-water instrument, and the above-water unit worked flawlessly and after the acquisition ended the data files were immediately transferred to the laptop for fast evaluation.

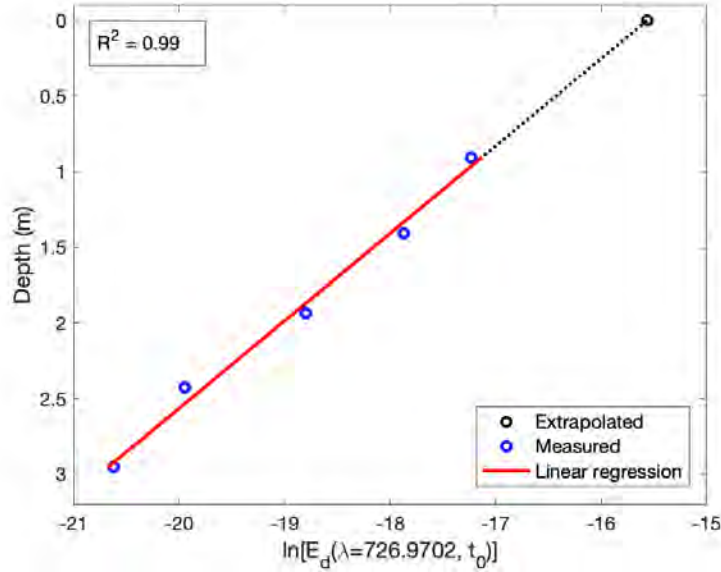


Figure 13: Best fit from the linear least-square regression of $\ln[E_d(z, \lambda, t_0)]$ against depth $1 < z < 3$ meters.

The dark subtraction of the radiance spectra resulted in negative radiance in the beginning and end of spectra, caused by weak signal and high noise, when using the maximum integration time of 10 seconds. The highest intensity recorded was 3800 digital counts (DC), but for a good recording should be about 14 000 DC. The spectrometer slit of 25 μm may be too small to receive enough signal. [Bongiorno \(2014\)](#) successfully used a downward-facing USB 2000+ spectrometer with slit 200 μm (340-1032 nm, Ocean Optics) together with a high sensitivity

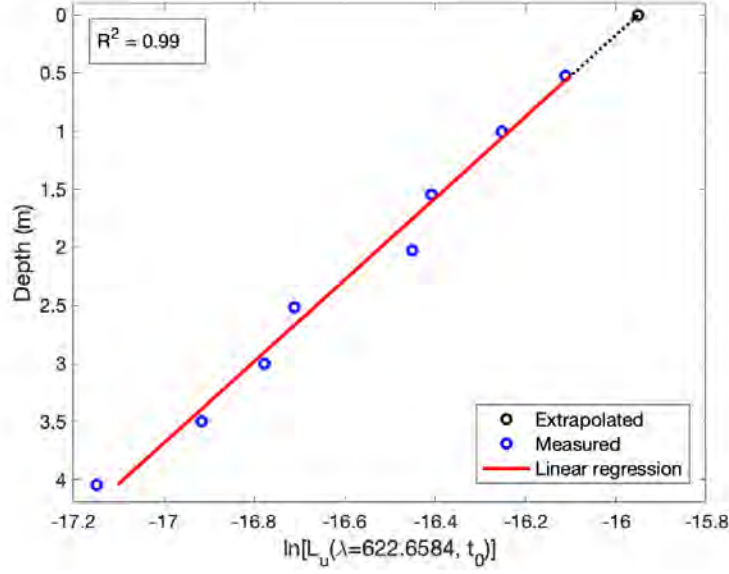


Figure 14: Best fit from the linear least-square regression of $\ln[L_u(z, \lambda, t_0)]$ against depth $0.5 < z < 4$ meters.

charge-coupled device (CCD) detector, for benthic mapping. Changing the slit size and using a higher sensitivity CCD could account for the low light levels underwater, resulting in a higher signal-to-noise ratio.

The linear regression analysis of $\ln[E_d(z, \lambda, t_0)]$ and $\ln[L_u(z, \lambda, t_0)]$ against depth produced a very good fit, average $R^2=0.92$ ($s=0.06$) and $R^2=0.94$ ($s=0.04$) respectively, showing best fits in figure 13 and 14.

Because of the reduced radiance wavelength range, only bands corresponding to OLCI bands Oa3-7 and Oa10 could be computed from the derived $\rho(\lambda)$. Hence, only one algorithm, CDOM7, could be validated (Tab. 3). The OpenSpecRad data with CDOM7 applied, resulted in $a_{CDOM}(443)=0.21 \text{ m}^{-1}$. The $a_{CDOM}(443)$ was underestimated by 74%, comparing to the measured $a_{CDOM}(443)=0.82$ from the water sample at 4 meters depth. Here, the time difference between the radiometric measurement and water sampling was only <1 hour, which further confirms the inaccurate fit of the algorithm. No validation statistics could be calculated since this only was one measurement ($N=1$).

The comparison between derived ρ_w for bands Oa3-7 and Oa10 and the corresponding OLCI ρ_w , resulted in an overestimation of 4-6 orders of magnitude. This could be a direct effect of only applying immersion factors for the radiance and not for the irradiance, resulting in

a division with small irradiance values. The irradiance calibration method could also have contributed.

The extrapolated $E_d(0^-, \lambda, t_0)$ only corresponded well to the above-water $E_d(0^+, \lambda, t_0)$ in wavelength range 405-700 nm (Fig. 15). The fluctuation in ranges 350-400 nm was introduced when applying the calibration, converting DC to absolute irradiance. The shorter wavelength range for $E_d(0^-, \lambda, t_0)$ was also caused by the calibration method. For using the comparison for detecting poor quality acquisitions, a proper irradiance calibration method must be used.

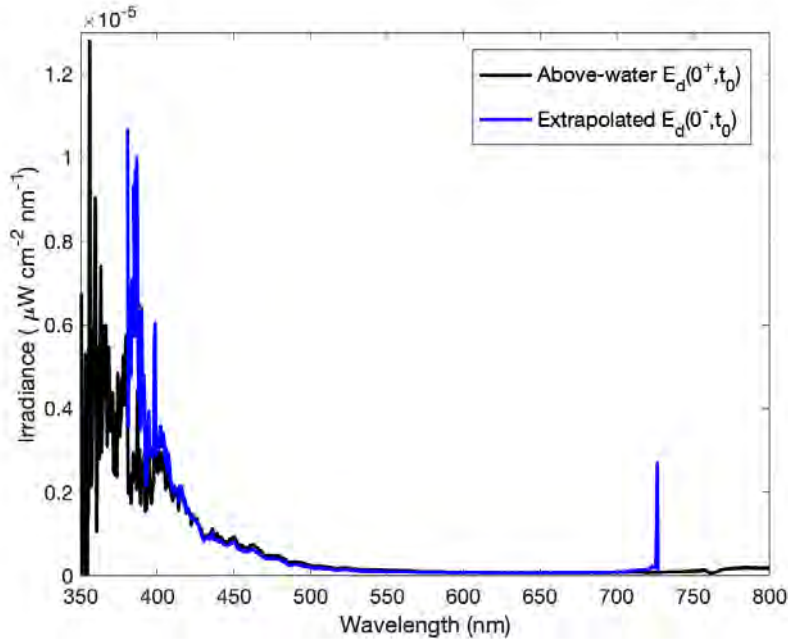


Figure 15: Comparison between the spectra of extrapolated $E_d(0^-, \lambda, t_0)$ and the above-water $E_d(0^+, \lambda, t_0)$.

The self-shading correction factors applied ranged from 1.06-1.79 (mean 1.12, $s=1.11$), meaning the radiance should have been underestimated with 6-79% if not corrected. The radius chosen to 2.5 centimeters was based on the distance from the center of the radiance sensor to the closest edge of the housing since the sensor not was positioned in the center of the housing. However, in equation 24 the sensor is assumed to be centered and this may have added error in the estimation. Also, the method by [Gordon and Ding \(1992\)](#) is more frequently used and would have been applied if the parameters were measured.

The immersion factors applied to the radiance measurement, ranging from 1.83-1.86, were similar to those found in [Ohde \(2003\)](#), ranging from 1.72-1.78, although the available n_g

values did not correspond to the curved dome glass of 6 mm thickness. To further improve the accuracy of the factors, they could be determined empirically together with the determination of the irradiance immersion factors, which were not resolved.

4 Conclusion

This study aimed to investigate the possibilities for CDOM bio-optical algorithms and radiometric measurements in the Kattegat, using Sentinel-3 OLCI satellite data and in situ data from the Open-source SpectroRadiometer (OpenSpecRad) system. The aim was also to build and provide guidance on how to build a low-cost in situ spectroradiometer system. Because of the large time difference between satellite overpass and in situ measurements, the locally fitted band-ratio algorithms for deriving $a_{CDOM}(443)$ did not produce a satisfying fit. Therefore, when performing the validation of the algorithms using both OLCI satellite data and OpenSpecRad data, the derived $a_{CDOM}(443)$ showed no correlation with in situ measurements and suffered from large scatter and overall error.

The cloud cover causing the large time difference highlights the challenges of satellite remote sensing of water quality parameters. The cloud coverage is the main weakness of satellite remote sensing in the Kattegat, as well as in northern Europe. However, in the near future two more Sentinel-3 OLCI satellites will be launched for collecting data, enhancing the availability of cloud-free images. Further research is needed to validate the band-ratio algorithms presented here, preferably with in situ measurements dedicated for Sentinel-3 OLCI overpass during good weather, which could not be met in this study.

However, for the first time it is showed that the OLCI ADG443 product has no correlation with $a_{CDOM}(443)$ in the Kattegat. Based on the results, the ADG443 product is not recommended for using as proxy for $a_{CDOM}(443)$ in the Kattegat.

The development of the OpenSpecRad system provides many solutions, as well as emphasizing the difficulties of performing accurate in situ radiometric measurements for deriving water-leaving reflectance, $\rho_w(\lambda)$. More work and adjustments are needed on the in-water instrument buoyancy, the downward facing radiance sensor, the absolute calibration, and the characterizations of immersion factors and self-shading correction factors. An addition

of accelerometers for pitch and roll would make it possible to exclude acquisitions with too much tilt, increasing the data quality. Finally, an inter-calibration with other radiometric instruments could be performed for estimation of measurement errors.

Using satellite remote sensing in the Kattegat could immensely increase the data availability for CDOM estimation and water quality monitoring. Hence, increasing the understanding for the global organic and inorganic carbon cycle. Since the OpenSpecRad system is low-cost and free for any one to build, it is pushing the limits for who can perform measurements and contribute to science.

Acknowledgements

Thank you to my supervisor Martin Hassellöv for making this project possible and giving me the opportunity to explore new fields within marine science. Thanks to the Kristineberg Center for Marine Research and Innovation for the financial contribution. A big thanks to Ursula Schwarz and the staff at Kristineberg Marine Research Station, University of Gothenburg, for helping out with the OpenSpecRad measurement and providing lab space and tools. I would like to thank Andrew King and Kai Sørensen at Norwegian Institute for Water Research (NIVA) for pre-processing and assembling the Ferrybox data. Thanks to Christoffer Wester at PLM Group for 3D-printing the underwater housings. Thank you to Susanne Kratzer for valuable feedback on the difficulties of in situ radiometric measurements. Thanks to Magnus Ljungström at KMG Fotonik and Evelien Huijs at Ocean Insight for the advice on spectroradiometer calibration. Thanks to all the people asking and answering questions about programming, Raspberry Pi, and DIY projects, openly on the internet and making the knowledge available. The biggest thanks to Kim for all the love and support and for always believing in me.

References

- E. Aas and B. Korsbø. Self-shading effect by radiance meters on upward radiance observed in coastal waters. *Limnology and Oceanography*, 42(5):968–974, 1997.
- P. Ammenberg, P. Flink, T. Lindell, D. Pierson, and N. Strombeck. Bio-optical modelling combined with remote sensing to assess water quality. *International Journal of Remote Sensing*, 23(8):1621–1638, 2002.

- R. H. Becker, M. Sayers, D. Dehm, R. Shuchman, K. Quintero, K. Bosse, and R. Sawtell. Unmanned aerial system based spectroradiometer for monitoring harmful algal blooms: A new paradigm in water quality monitoring. *Journal of Great Lakes Research*, 45(3):444–453, 2019.
- J. F. Berthon, F. Mélin, and G. Zibordi. Ocean colour remote sensing of the optically complex european seas. In *Remote Sensing of the European Seas*, pages 35–52. Springer Netherlands, Dordrecht, 2008.
- G. Björk and K. Nordberg. Upwelling along the Swedish west coast during the 20th century. *Continental Shelf Research*, 23(11):1143–1159, 2003.
- K. Blix, K. Pálffy, V. Tóth, and T. Eltoft. Remote sensing of water quality parameters over Lake Balaton by using Sentinel-3 OLCI. *Water (Switzerland)*, 10(10), 2018.
- Blue Robotics. ms5837-python [software]. <https://github.com/bluerobotics/ms5837-python>, 2017. Available online. Accessed on 20 May 2020.
- V. Boddula, L. Ramaswamy, and D. Mishra. Cyanosense: A wireless remote sensor system using raspberry-pi and arduino with application to algal bloom. In *2017 IEEE International Conference on AI & Mobile Services (AIMS)*, pages 85–88. IEEE, 2017.
- D. L. Bongiorno. *Hyperspectral benthic mapping from underwater robotic platforms*. PhD thesis, University of Sydney, Faculty of Engineering & IT, School of Aerospace, Mechanical and Mechatronic Engineering, 2014.
- P. Brezonik, K. D. Menken, and M. Bauer. Landsat-based Remote Sensing of Lake Water Quality Characteristics, Including Chlorophyll and Colored Dissolved Organic Matter (CDOM). *Lake and Reservoir Management*, 21(4):373–382, 2005.
- P. L. Brezonik, L. G. Olmanson, J. C. Finlay, and M. E. Bauer. Factors affecting the measurement of CDOM by remote sensing of optically complex inland waters. *Remote Sensing of Environment*, 157:199–215, 2015.
- A. Bricaud, A. Morel, and L. Prieur. Absorption by dissolved organic matter of the sea (yellow substance) in the UV and visible domains. *Limnology and Oceanography*, 26(1):43–53, 1981.
- C. N. Brooks, A. G. Grimm, A. M. Marcarelli, and R. J. Dobson. Multiscale collection and analysis of submerged aquatic vegetation spectral profiles for Eurasian watermilfoil detection. *Journal of applied remote sensing*, 13(3):037501–037501, 2019.
- A. Burkart, S. Cogliati, A. Schickling, and U. Rascher. A Novel UAV-Based Ultra-Light Weight Spectrometer for Field Spectroscopy. *IEEE Sensors Journal*, 14(1):62–67, 2014.
- B. T. Champion, M. Jamshidi, and M. A. Joordens. 3d printed underwater housing. In *2016 World Automation Congress (WAC)*, volume 2016, pages 1–6, 2016.

- C. Donlon, B. Berruti, A. Buongiorno, M.-H. Ferreira, P. Féménias, J. Frerick, P. Goryl, U. Klein, H. Laur, C. Mavrocordatos, J. Nieke, H. Rebhan, B. Seitz, J. Stroede, and R. Sciarra. The Global Monitoring for Environment and Security (GMES) Sentinel-3 mission. *Remote Sensing of Environment*, 120:37–57, 2012. The Sentinel Missions - New Opportunities for Science.
- D. Doxaran, R. C. N. Cherukuru, and S. J. Lavender. Use of reflectance band ratios to estimate suspended and dissolved matter concentrations in estuarine waters. *International Journal of Remote Sensing*, 26(8): 1763–1769, 2005.
- EUMETSAT. Sentinel-3 OLCI Marine User Handbook. http://www.eumetsat.int/website/wcm/idc/idcplg?IdcService=GET_FILE&dDocName=PDF_DMT_907205&RevisionSelectionMethod=LatestReleased&Rendition=Web, 2018. EUM/OPS-SEN3/MAN/17/907205. Available online. Accessed on 3 September 2019.
- H. R. Gordon and K. Ding. Self-shading of in-water optical instruments. *Limnology and Oceanography*, 37(3): 491–500, 1992.
- S. Groom, S. Sathyendranath, Y. Ban, S. Bernard, R. Brewin, V. Brotas, C. Brockmann, P. Chauhan, J.-K. Choi, A. Chuprin, S. Ciavatta, P. Cipollini, C. Donlon, B. Franz, X. He, T. Hirata, T. Jackson, M. Kampel, H. Krasemann, S. Lavender, S. Pardo-Martinez, F. Mélin, T. Platt, R. Santoleri, J. Skakala, B. Schaeffer, M. Smith, F. Steinmetz, A. Valente, and M. Wang. Satellite Ocean Colour: Current Status and Future Perspective. *Frontiers in Marine Science*, 6, 2019.
- J. Grósz, I. Waltner, and Z. Vekerdy. First analysis results of in situ measurements for algae monitoring in Lake Naplås (Hungary). *Carpathian Journal of Earth and Environmental Sciences*, 14(2):385–398, 2019.
- E. T. Harvey, S. Kratzer, and A. Andersson. Relationships between colored dissolved organic matter and dissolved organic carbon in different coastal gradients of the Baltic Sea. *AMBIO*, 44(3):392401, 2015.
- S. B. Hooker, G. Zibordi, J.-F. Berthon, and J. W. Brown. Above-water radiometry in shallow coastal waters. *Applied Optics*, 43(21):4254, 2004.
- N. Højerslev, N. Holt, and T. Aarup. Optical measurements in the North Sea-Baltic Sea transition zone. I. On the origin of the deep water in the Kattegat. *Continental Shelf Research*, 16(10):1329–1342, 1996.
- K. Kallio, J. Attila, P. Härmä, S. Koponen, J. Pulliainen, U.-M. Hyytiäinen, and T. Pyhälähti. Landsat ETM+ Images in the Estimation of Seasonal Lake Water Quality in Boreal River Basins. *Environmental Management*, 42(3):511–522, 2008.
- S. Kay, J. Hedley, and S. Lavender. Sun Glint Correction of High and Low Spatial Resolution Images of Aquatic Scenes: a Review of Methods for Visible and Near-Infrared Wavelengths. *Remote Sensing*, 1(4): 697–730, 2009.

- J. T. O. Kirk. *Light and photosynthesis in aquatic ecosystems*. Cambridge University Press, Cambridge, 3rd ed. edition, 2011.
- Ø. Kleiv, A. Folkestad, J. Høkedal, K. Sørensen, and E. Aas. Estimation of upward radiances and reflectances at the surface of the sea from above-surface measurements. *Ocean Science*, 11(5):779, 2015.
- Knight Optical. Optical Glasses: Visible - Near Infra-Red, Schott N-BK7 for 250nm-2500nm transmission. <https://www.knightoptical.com/wp-content/uploads/2020/02/Opticalglass-Schott-N-BK7.pdf>, 2020. Available online. Accessed on 2 August 2020.
- S. Koponen, J. Attila, J. Pulliainen, K. Kallio, T. Pyhälähti, A. Lindfors, K. Rasmus, and M. Hallikainen. A case study of airborne and satellite remote sensing of a spring bloom event in the Gulf of Finland. *Continental Shelf Research*, 27(2):228–244, 2007.
- P. Kowalczyk, J. Olszewski, M. Darecki, and S. Kaczmarek. Empirical relationships between coloured dissolved organic matter (CDOM) absorption and apparent optical properties in Baltic Sea waters. *International Journal of Remote Sensing*, 26(2):345–370, 2005.
- P. Kowalczyk, M. Darecki, M. Zablocka, and I. Gorecka. Validation of empirical and semi-analytical remote sensing algorithms for estimating absorption by Coloured Dissolved Organic Matter (CDOM) in the Baltic Sea from SeaWiFS and MODIS imagery. *Oceanologia*, 52(2):171–196, 2010.
- S. Kratzer and G. Moore. Inherent optical properties of the Baltic Sea in comparison to other seas and oceans. *Remote Sensing*, 10(3):418–446, 2018.
- S. Kratzer, E. T. Harvey, and P. Philipson. The use of ocean color remote sensing in integrated coastal zone management — A case study from Himmerfjärden, Sweden. *Marine Policy*, 43:29–39, 2014.
- S. Kratzer, P. Kowalczyk, and S. Sagan. Bio-optical Water Quality Assessment. In *Biological Oceanography of the Baltic Sea*, pages 527–545. Springer Netherlands, 2017.
- T. Kutser, D. C. Pierson, K. Y. Kallio, A. Reinart, and S. Sobek. Mapping lake cdom by satellite remote sensing. *Remote Sensing of Environment*, 94(4):535–540, 2005.
- T. Kutser, T. Soomets, K. Toming, R. Uiboupin, A. Arikas, K. Vahter, and B. Paavel. Assessing the Baltic Sea Water Quality with Sentinel-3 OLCI Imagery. In *BALTIC*, pages 1–6, 6 2018.
- D. Kyrliuk. *Baltic Sea from Space: The use of ocean colour data to improve our understanding of ecological drivers across the Baltic Sea basin – algorithm development, validation and ecological applications*. PhD thesis, Department of Ecology, Environment and Plant Sciences, Stockholm University, Stockholm, 2019.
- D. Kyrliuk and S. Kratzer. Evaluation of Sentinel-3A OLCI Products Derived Using the Case-2 Regional CoastColour Processor over the Baltic Sea. *Sensors*, 19(16), 2019.

- W. Li, L. Tian, S. Guo, J. Li, Z. Sun, and L. Zhang. An automatic stationary water color parameters observation system for shallow waters: Designment and applications. *Sensors*, 19(20), 2019.
- Libusb. Libusb 0.1.12 [software]. <https://sourceforge.net/projects/libusb/>, 2006. Available online. Accessed on 2 December 2019.
- M. Ligi, T. Kutser, K. Kallio, J. Attila, S. Koponen, B. Paavel, T. Soomets, and A. Reinart. Testing the performance of empirical remote sensing algorithms in the Baltic Sea waters with modelled and in situ reflectance data. *Oceanologia*, 59(1):57–68, 2017.
- H. Loisel, V. Vantrepotte, C. Jamet, and D. N. Dat. Challenges and New Advances in Ocean Color Remote Sensing of Coastal Waters. In E. Zambianchi, editor, *Topics in Oceanography*, chapter 4. IntechOpen, Rijeka, 2013.
- A. Mannino, M. G. Novak, S. B. Hooker, K. Hyde, and D. Aurin. Algorithm development and validation of CDOM properties for estuarine and continental shelf waters along the northeastern U.S. coast. *Remote Sensing of Environment*, 152(C):576–602, 2014.
- Markforged. Composites - Data sheet. <http://static.markforged.com/downloads/composites-data-sheet.pdf>, 2020. Available online. Accessed on 5 March 2020.
- B. Matsushita, W. Yang, P. Chang, F. Yang, and T. Fukushima. A simple method for distinguishing global Case-1 and Case-2 waters using SeaWiFS measurements. *ISPRS Journal of Photogrammetry and Remote Sensing*, 69(C):74–87, 2012.
- K. D. Menken, P. L. Brezonik, and M. E. Bauer. Influence of Chlorophyll and Colored Dissolved Organic Matter (CDOM) on Lake Reflectance Spectra: Implications for Measuring Lake Properties by Remote Sensing. *Lake and Reservoir Management*, 22(3):179–190, 2006.
- D. Mishra, I. Ogashawara, and A. Gitelson. *Bio-optical Modeling and Remote Sensing of Inland Waters*. Elsevier Inc., Amsterdam, Netherlands, 05 2017.
- C. D. Mobley. The optical properties of water. In *Handbook of Optics, 2nd edn., Vol. 1*, page 43.3–43.56. McGraw-Hill, New York, 1995.
- C. D. Mobley. Estimation of the Remote-Sensing Reflectance from Above-Surface Measurements. *Applied optics*, 38(36):7442–55, 1999.
- A. Morel, D. Antoine, and B. Gentili. Bidirectional reflectance of oceanic waters: accounting for Raman emission and varying particle scattering phase function. *Applied Optics*, 41(30):6289, 2002.
- J. H. Morrow, S. B. Hooker, C. R. Booth, G. Bernhard, R. N. Lind, and J. W. Brown. Advances in

- Measuring the Apparent Optical Properties (AOPs) of Optically Complex Waters. Technical Memorandum 2010-215856, NASA Goddard Space Flight Center, Greenbelt, MD, United States, 2010.
- Ocean Optics. STS Developer’s Kit - Connect, Code, Create – Right Out of the Box (Product Sheet), 2014. Available online. Accessed on 22 October 2019.
- Ocean Optics. STS Developer’s Kit - Installation and Operation Manual, 2015. DEV-RASPI-KIT-02-201512b. Available online. Accessed on 29 November 2019.
- Ocean Optics. SeaBreeze 3.0.11 [software]. <https://sourceforge.net/projects/seabreeze/>, 2016a. Available online. Accessed on 2 December 2019.
- Ocean Optics. SeaBreeze API documentation. <https://www.oceaninsight.com/globalassets/catalog-blocks-and-images/software-downloads-installers/javadocs-api/seabreeze/html/index.html>, 2016b. Available online. Accessed on 2 December 2019.
- I. Ogashawara. Terminology and classification of bio-optical algorithms. *Remote Sensing Letters*, 6(8):613–617, 2015.
- T. Ohde. Derivation of immersion factors for the hyperspectral trios radiance sensor. *Journal of Optics A: Pure and Applied Optics*, 5(3):L12–L14, 2003.
- J. E. O’Reilly. SeaWiFS Postlaunch Calibration and Validation Analyses, Part 3. NASA Technical Memorandum 2000-206892, Vol. 11, S.B. Hooker and E.R. Firestone, Eds., NASA Goddard Space Flight Center, Greenbelt, MD, United States, 2000.
- C. L. Osburn and C. A. Stedmon. Linking the chemical and optical properties of dissolved organic matter in the baltic–north sea transition zone to differentiate three allochthonous inputs. *Marine Chemistry*, 126(1-4):281–294, 2011.
- T. Persson and M. Wedborg. Multivariate evaluation of the fluorescence of aquatic organic matter. *Analytica Chimica Acta*, 434(2):179–192, 2001.
- R. Preisendorfer. *Application of Radiative Transfer Theory to Light Measurements in the Sea*. Institut Géographique National, 1961.
- Raspberry Pi Foundation. Setting up a Raspberry Pi as a routed wireless access point. <https://www.raspberrypi.org/documentation/configuration/wireless/access-point-routed.md>, 2019. Available online. Accessed on 2 December 2019.
- Sea-Bird Scientific. DataSheet - Profiler II Free-Falling Optical Profiler, 2017. Available online. Accessed on 5 November 2019.

- M. Seelye. *An Introduction to Ocean Remote Sensing*. Cambridge University Press, second edition, 2014.
- Z. Shang, Z. Lee, Q. Dong, and J. Wei. Self-shading associated with a skylight-blocked approach system for the measurement of water-leaving radiance and its correction. *Applied optics*, 56(25):7033, 2017.
- R. C. Smith and K. S. Baker. The Analysis Of Ocean Optical Data. In M. A. Blizard, editor, *Ocean Optics VII*, volume 0489, pages 119–126. International Society for Optics and Photonics, SPIE, 1984.
- K. Sørensen, E. Aas, and J. Høkedal. Validation of MERIS water products and bio-optical relationships in the Skagerrak. *International Journal of Remote Sensing: MERIS (MEdium Resolution Imaging Spectrometer)*, 28(3-4):555–568, 2007.
- C. A. Stedmon, S. Markager, and R. Bro. Tracing dissolved organic matter in aquatic environments using a new approach to fluorescence spectroscopy. *Marine Chemistry*, 82(3):239–254, 2003.
- C. A. Stedmon, C. L. Osburn, and T. Kragh. Tracing water mass mixing in the Baltic–North Sea transition zone using the optical properties of coloured dissolved organic matter. *Estuarine, Coastal and Shelf Science*, 87(1):156–162, 2010.
- Y. Q. Tian, Q. Yu, and W. Zhu. Estimating of chromophoric dissolved organic matter (CDOM) with in-situ and satellite hyperspectral remote sensing technology. In *2012 IEEE International Geoscience and Remote Sensing Symposium*, pages 2040–2042. IEEE, 2012.
- K. Töming, T. Kutser, A. Arikas, K. Vahter, and B. Paavel. Mapping Water Quality Parameters with Sentinel-3 Ocean and Land Colour Instrument imagery in the Baltic Sea. *Remote Sensing*, 9(10):1070, 2017.
- G. Zibordi and G. Ferrari. Instrument self-shading in underwater optical measurements: experimental data. *Applied Optics*, 34(15):2750, 1995.
- G. Zibordi, S. Hooker, J. Mueller, and G. Lazin. Characterization of the immersion factor for a series of in-water optical radiometers. *Journal of Atmospheric and Oceanic Technology*, 21(3):501–514, 2004.
- G. Zibordi, K. Ruddick, I. Ansko, G. Moore, S. Kratzer, J. Icely, and A. Reinart. In situ determination of the remote sensing reflectance: an inter-comparison. *Ocean Science Discussions*, 9(2):787–833, 2012.

Appendix A Building the OpenSpecRad

A.1 Hardware Assembly

The hardware assembly was based on the STS Developer's Kit from Ocean Optics (now Ocean Insight), which includes a miniature spectrometer, Raspberry Pi (RPi) 1B+ single-board computer with a Wi-Fi dongle and an 8 GB micro Secure Digital (SD) card with pre-installed software and drivers, and a 3 ampere-hours (Ah) battery ([Ocean Optics, 2014, 2015](#)). However, all the parts were bought separately since later versions of the RPi have built-in WiFi, the spectrometer device driver was open-source and a more powerful battery was preferred.



Figure 16: The miniature spectrometer STS-VIS (42x40x24 mm) coupled to the single-board computer Raspberry Pi 3B+ (94x63x32 mm) coupled to a 10 Ah battery.

Three RPi 3B+ (Raspberry Pi Foundation), including a 16 GB micro SD card with the New Out Of Box Software (NOOBS) operating system installer, were each coupled to a miniature spectrometer (STS-VIS, 350-800 nm, 25 μm slit, 1.5 nm resolution, Ocean Optics) (Fig. 16). Each RPi was powered by a 10 Ah battery.

An inter-integrated circuit (I^2C) real-time clock (RTC) (High Accuracy Pi RTC DS3231,



Figure 17: The above-water $E_d(0^+, \lambda)$ unit in its box, with the spectroradiometer sticking out in the top left and the Raspberry Pi in the bottom right with the real-time clock attached. The battery is placed underneath the Raspberry Pi.

Seed Studio) with a 3 V CR1225 button cell battery was connected to the above-water unit $E_d(0^+, \lambda)$ (Fig. 17). The RTC was simply pushed directly onto the general-purpose input/output (GPIO) pins GPIO2 (serial data line, SDA), GPIO3 (serial clock line, SCL), 3.3V power pin, and ground pin.

The I²C pressure sensors (Bar30-Sensor-R1-RP, 2 mm depth resolution, Blue Robotics) were each connected to the in-water units $E_d(z, \lambda)$ and $L_u(z, \lambda)$, using an I²C level converter (Blue Robotics) (Fig. 18). Header pins (0.1") were soldered onto each of the converters and the jumper solder was soldered for 3.3 V. The converters were used to break out of the DF13 connectors of the pressure sensors for connecting to the RPis. Jumper wires were used for connecting the converters via their header pins to the RPi pins stated before. The converters were each taped to the insides of the RPi cases.

The spectrometer used for measuring the L_u was equipped with an empty barrel (NA=0.22), attached with a cut-off spectrometer lid, with a full-angle field-of-view (FAFOV) of 25°. The two E_d spectrometers each had a cosine corrector (CC-3-DA Spectralon diffuser, Ocean Optics) directly screwed onto the spectrometer, creating a FAFOV of 180°.

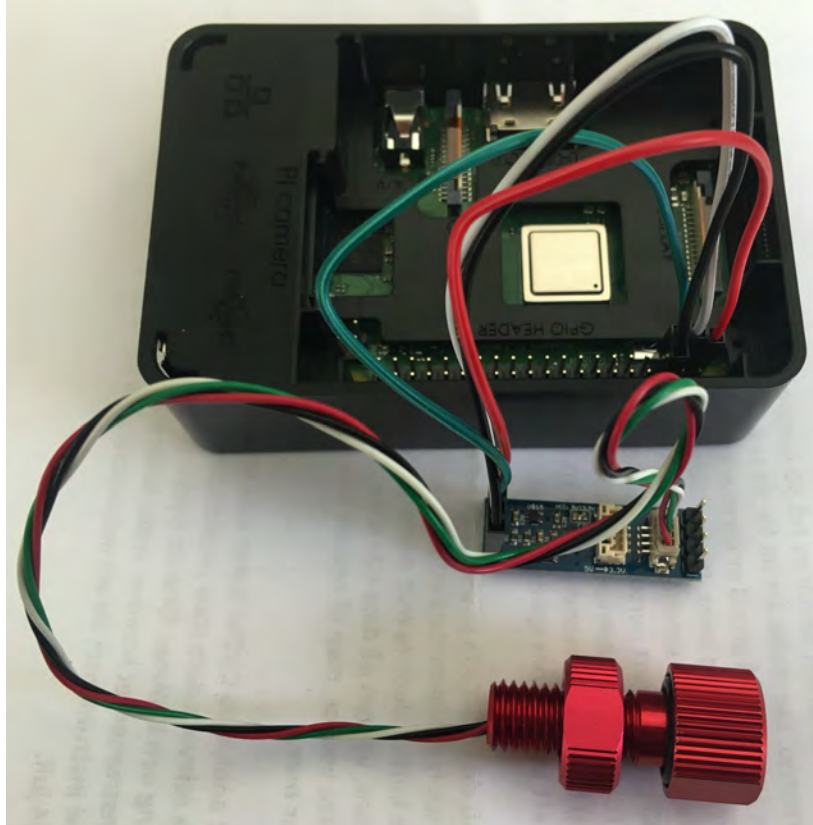


Figure 18: The Raspberry Pi 3B+ coupled to the pressure sensor via the I²C level converter through four jumper wires.

A.2 Software Configurations

The operating system Raspbian Stretch 9 was installed through the operating system installer NOOBS. The USB communication library Libusb (version 0.1.12, [Libusb, 2006](#)) was installed together with the open-source spectrometer device driver library SeaBreeze (version 3.0.11, [Ocean Optics, 2016a](#)) for Ocean Optics spectrometers, following the instructions in the SeaBreeze application programming interface (API) documentation ([Ocean Optics, 2016b](#)). In the RPi Configuration Tool, the I²C was enabled and the i2c-tools program was installed. This enabled communication between the RPi and the RTC or the RPi and the pressure sensor. The date and time were configured to be kept by the RTC. The supplied C and C++ sample code included in SeaBreeze was used as a starting point for developing a C program for making spectral measurements, using the integrated development environment (IDE) Geany (version 1.29) installed with the operating system.

For controlling the spectroradiometer system wirelessly via laptop, the RPi was set up as a routed wireless access point with a static internet protocol (IP) address, according to the

Raspberry Pi documentation ([Raspberry Pi Foundation, 2019](#)). The secure shell (SSH) was enabled in the RPi Configuration Tool for accessing the command-line of the RPi from the laptop via connecting to its Wi-Fi network. An SSH key was also set up between the RPi and the laptop for passwordless access. Unique IP addresses were reserved for the in-water units based on their unique MAC addresses, so they were assigned the same IP addresses every time they connected, which facilitated the communication via SSH. When the in-water units are connected to the above-water network their respective command-lines can be accessed from the laptop via double SSH via the shared network.

The above-water unit RPi SD card, which contained all software and configurations, was then cloned to both in-water unit SD cards. The wireless access point service was disabled and the Wi-Fi settings reverted to the operating system default. Every time the in-water unit connected to the above-water network the date and time were synced. The SSH key was replaced with a new one for each in-water unit. A Python program was developed in the Python IDE Thonny (version 2.1.16) for managing the communication with the pressure sensor, using the library MS5837-python ([Blue Robotics, 2017](#)). The python program was then embedded into the measurement program running the spectral measurement.

A shell program was developed for controlling the spectroradiometer system from the laptop, e.g. starting the measurement programs, detecting errors, and transferring the collected data remotely via SSH. The measurement parameters, e.g. integration time, minimum depth for the first measurement, and depth resolution, were read from separate files when starting the three radiometric acquisitions, making changes of parameters easy.

A.3 Housing and Frame Construction

Based on the in-water units, a 3D-drawing of the waterproof and pressure-proof housing was designed using the computer-aided design (CAD) software Fusion 360 (2.0.8176, Autodesk) (Fig. 19 and 20). The hardware was arranged so that the housing outer diameter was as small as possible, while not exceeding the maximum print dimensions of the 3D-printer (320x132x154 mm). The inside was designed so the hardware was held in position by each other (Fig. 21 and 22). Two identical cylindrical housings (maximum dimensions 132x132x154 mm) and two threaded lids were printed by PLM Group in Värnamo on the

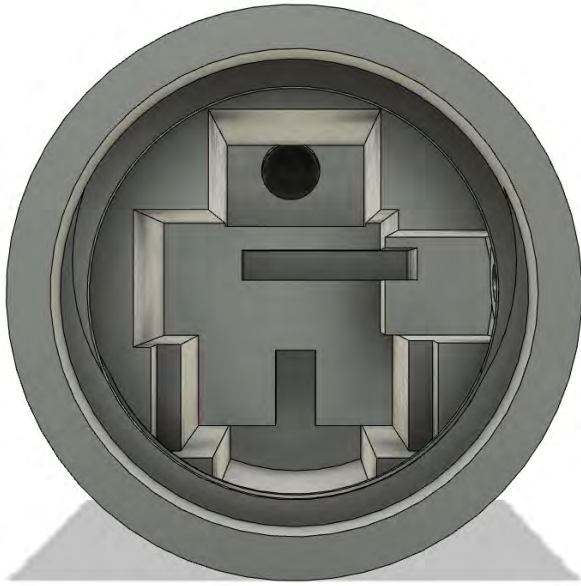


Figure 19: 3D-drawing of the inside structure of the housing.



Figure 20: 3D-drawing of the the housing with the borosilicate crown glass dome in the front.

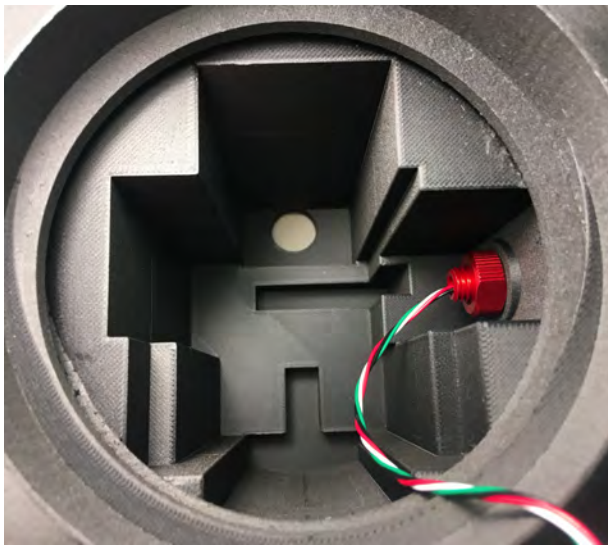


Figure 21: The inside structure of the 3D-printed housing with the pressure sensor mounted with a nut from the inside.



Figure 22: All the hardware and cables mounted inside the housing, with the spectroradiometer on top, the Raspberry Pi in the middle, the battery in the bottom and, the pressure sensor to the right.

desktop 3D-printer Mark Two (Markforged) using the material Onyx, with 0.8 mm massive outer layer and triangular infill. Onyx is a mixture of nylon and chopped carbon fibers and is 40% stronger and stiffer than ABS ([Markforged, 2020](#)). The print time for one housing and one lid was 3.7 days and 22 h, respectively. The printing support material was removed

and the threads were ground to ease the opening and closing of the housings. The in-water units were put into separate housings to limit the damage in case of leakage. All surfaces but the thread and inside of the housings were laminated with epoxy (NM Laminering 635, NM Hårdare 650M, Nils Malmgren AB) to protect the material from absorbing water. The epoxy hardened for 24 hours at room temperature and for 16 hours at 50 °C. Custom borosilicate crown glass domes (6 mm thick, Schott N-BK7, Knight Optical) were attached to each of the housing front openings using polyurethane-based glue (Sikaflex 591, Sika).

To ensure the housings were waterproof two grooves for placing o-rings were included in the lid design (Fig. 23). However, the o-rings were too hard and could not be squeezed into the housing when closing the lid. The grooves were carefully ground, resulting in a smaller squeeze of the o-rings, but the housings were not watertight. Instead, silicone gaskets (3 mm thick) were cut from a sheet and placed in the outer groove on the lid and sealing tape wrapped inside the tread.

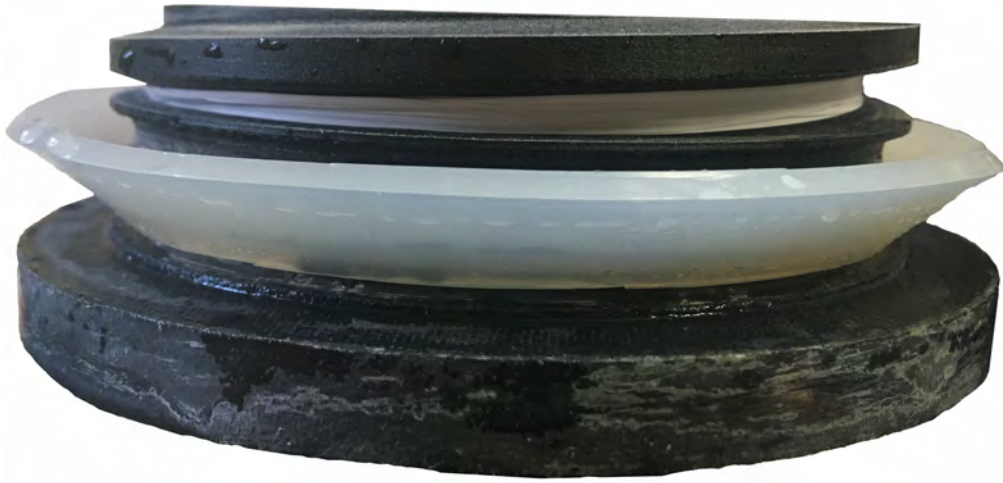


Figure 23: The housing lid with the thread with white sealing tape in the top, one empty groove and the silicone gasket placed in the the other groove.

The housings were mounted onto a custom stainless steel frame (maximum dimensions 800x140x25 mm, Westers Mekaniska AB) using hose clamps. The housings were directed in opposite directions, with the $L_u(z, \lambda)$ housing rotated so that the dome was placed closest to the edge of the instrument, reducing self-shading (Fig. 24). Diving weights (2 kg) were mounted on the steel frame bottom with hose clamps (Fig. 1). The rope was attached to the steel frame top and winded onto the reel.

Silicone grease was applied onto the pressure sensor o-rings before mounting into the housing side holes by tightening the nuts from the insides (Fig. 21). The rest of the $E_d(z, \lambda)$ and $L_u(z, \lambda)$ units were put inside their respective housings, with the spectroradiometers looking out through the domes. The total weight of the in-water instrument was 6 kg.

The above-water $E_d(0^+, \lambda)$ unit was put in a plastic box for protection from water splash, with the spectroradiometer looking out on the side (Fig. 17).

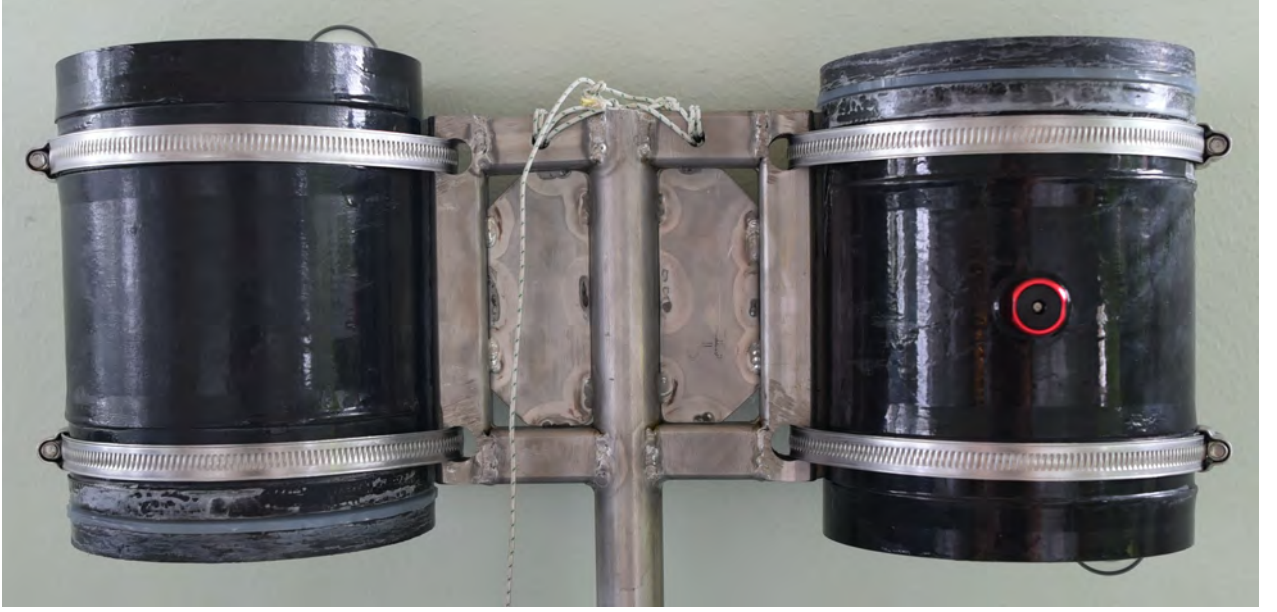


Figure 24: The housings with the lids closed mounted on the steel frame. The left housing holds the $E_d(z, \lambda)$ unit and the right housing holds the $L_u(z, \lambda)$ unit. The $E_d(z, \lambda)$ housing pressure sensor is sticking out on the backside.